CD4+ T cell-induced inflammatory killing controls immune evasive tumours

Thomas Tüting (thomas.tueting@med.ovgu.de)
University Hospital Magdeburg https://orcid.org/0000-0001-7146-0934

Bastian Kruse
University Hospital Magdeburg

Anthony Buzzai
University Hospital Magdeburg

Naveen Shridhar
University Hospital Magdeburg

Andreas Braun
University Hospital Magdeburg https://orcid.org/0000-0002-6954-0633

Susan Gellert
University Hospital Magdeburg

Kristin Knauth
University Hospital Magdeburg

Johannes Peters
University Hospital Magdeburg

Janne Ruotsalainen
University Hospital Magdeburg

Miriam Mengoni
University Hospital Magdeburg

Tetje van der Sluis
University Hospital Magdeburg https://orcid.org/0000-0003-1804-1647

Anna Krone
University Hospital Magdeburg

Di Yu
Uppsala University https://orcid.org/0000-0002-8636-0351

Simon Höhn
University Hospital Magdeburg

Yan Fu
University Hospital Magdeburg

Magnus Essand
https://orcid.org/0000-0002-9725-0422

Robert Geffers

Helmholtz Centre for Infection Research, Braunschweig https://orcid.org/0000-0003-4409-016X
Dimitrios Mougiakakos
University of Madgeburg
Sascha Kahlfuß
University Hospital Magdeburg
Hamid Kashkar
CECAD Research Center https://orcid.org/0000-0003-2796-1429
Evelyn Gaffal
University Hospital Magdeburg
Wolfgang Kastenmüller
University of Würzburg https://orcid.org/0000-0002-3835-1485
Andreas Müller
Otto-von-Guericke-University Magdeburg https://orcid.org/0000-0002-0281-6383

Biological Sciences - Article

Keywords:

Posted Date: June 29th, 2022

DOI: https://doi.org/10.21203/rs.3.rs-1764653/v1

Title

CD4+ T cell-induced inflammatory killing controls immune evasive tumours

Authors

Bastian Kruse[1,8], Anthony Buzzai[1,8], Naveen Shridhar[1,8], Andreas Braun[1], Susan Gellert[1], Kristin Knauth[1], Johannes Peters[1], Janne Ruotsalainen[1], Miriam Mengoni[1], Tetje Cornelia van der Sluis[1], Simon Höhn[1], Anna Krone[2], Yan Fu[2], Di Yu[3], Magnus Essand[3], Robert Geffers[4], Dimitrios Mougiakakos[5], Sascha Kahlfuß[2], Hamid Kashkar[6], Evelyn Gaffal[1], Wolfgang Kastenmüller[7], Andreas J. Müller[2,9*], Thomas Tüting[1,9*]

Affiliations

[1]Laboratory of Experimental Dermatology, Department of Dermatology, University Hospital and Health Campus Immunology Infectiology and Inflammation (GC-I3), Otto-von-Guericke-University, Magdeburg, Germany

[2]Institute of Molecular and Clinical Immunology, Health Campus Immunology Infectiology and Inflammation (GC-I3), Otto-von-Guericke-University, Magdeburg, Germany

[3]Department of Immunology, Genetics and Pathology, Uppsala University, Uppsala, Sweden

[4]Helmholtz Centre for Infection Research, Braunschweig, Germany

[5]Department of Hematology, University Hospital and Health Campus Immunology Infectiology and Inflammation (GC-I3), Otto-von-Guericke-University, Magdeburg, Germany

[6]Institute for Molecular Immunology, Centre for Molecular Medicine Cologne and Cologne Excellence Cluster on Cellular Stress Responses in Ageing-Associated Diseases, University of Cologne, Cologne, Germany

[7]Institute for Systems Immunology, Würzburg, Germany

[8]These authors contributed equally to this work: Bastian Kruse, Anthony Buzzai, Naveen Shridhar.

[9]These authors jointly supervised this work: Andreas J. Müller, Thomas Tüting

[*]e-mail: andreas.mueller@med.ovgu.de; thomas.tueting@med.ovgu.de

Summary

Current clinically applied cancer immunotherapies largely focus on the ability of CD8+ cytolytic T-cells to directly recognise and kill tumour cells[1–3]. These strategies are limited by the emergence of MHC-I-deficient or IFN-unresponsive tumour cells and the development of an immunosuppressive tumour microenvironment[4–6]. CD4+ effector T-cells can contribute to tumour immune defence independent of CD8+ T-cells. However, the potential and the mechanisms of CD4+ T-cell-mediated anti-tumour immunity are incompletely understood[7–12]. Here, we show how an indirect CD4+ T-cell-mediated mode of action, that is fundamentally different from CD8+ T-cells, enables the eradication of tumours that would otherwise escape direct T-cell targeting. CD4+ effector T-cells preferentially cluster at tumour invasive margins where they engage in antigen-specific interactions with MHC-II+CD11c+ cells, while CD8+ T-cells briskly infiltrate tumour tissues. CD4+ T-cells and innate immune stimulation reprogram the tumour-associated inflammatory monocyte network towards IFN-activated antigen-presenting and tumouricidal effector phenotypes. This results in an amplification loop driving the release of T-cell-derived IFNγ and myeloid cell-derived nitric oxide which cooperatively induce apoptotic death of MHC-deficient and IFN-unresponsive tumour cells that escape cytolytic CD8+ T-cell therapy. Exploiting the ability of CD4+ T-cells to orchestrate indirect inflammatory killing of tumour cells complements the direct cytolytic activity of T-cells to advance cancer immunotherapies.

Introduction

Initial proof-of-principle for the clinical efficacy of T-cell immunotherapy was provided by adoptive cell therapies (ACT) utilising *ex vivo* expanded tumour-infiltrating lymphocytes for patients with metastatic melanoma[13]. The success of monoclonal antibodies that target the immunoregulatory receptors CTLA4 and PD1, an approach now called immune checkpoint blockade, paved the way for the clinical breakthrough of T-cell-directed immunotherapies[14]. The efficacy of both strategies is mainly attributed to the reactivation of CD8+ T-cells that specifically recognise tumour antigens in the form of MHC-I-bound peptide epitopes on tumour cell surfaces. Following antigen-recognition, CD8+ T-cells release cytolytic granules that initiate apoptotic death of target cells. Accordingly, most approaches to improve cancer immunotherapy focus on strategies to further augment their cytolytic effector functions in tumour tissues. At the same time, these efforts are antagonised by the emergence of MHC-I-deficient or IFN-unresponsive tumour cell clones that escape the recognition and destruction by cytolytic T-cells[4,5].

Recently, single cell transcriptional profiling of tumour-infiltrating immune cell landscapes provided new insights into the composition and the functional states of T-cells within tumour tissues. These studies not only characterised CD4+ T-cells with helper and regulatory phenotypes, but also revealed the presence of CD4+ T-cells with cytolytic effector phenotypes that were able to directly recognise and kill MHC-II-expressing malignant cells[9–11]. This has reignited interest to understand how CD4+ T-cells contribute to tumour immunity independent of CD8+ T-cells[15–18]. Historically, CD4+ T-cells were first shown to control tumours even in the absence of direct recognition and cytolytic destruction of target cells. More than 50 years ago, it was reported that immune lymphoid cells cooperate with mononuclear phagocytes and provide protection not only against an infection with bacterial pathogens, but also against a challenge with tumour cells[19,20]. Subsequent work over the next three decades revealed shared cellular and molecular mechanisms of immune defence against pathogens and tumours, including indirect activation of CD4+ effector T-cells by MHC-II-expressing professional antigen-presenting cells, the secretion of IFNγ and the production of nitric oxide by IFN-activated macrophages[21–23]. However, the spatiotemporal dynamics of CD4 T-cells and the site of action within the tumour tissue have not been investigated.

With the advent of adoptive cell therapies and immune checkpoint blockade, the main research focus shifted towards understanding CD8+ cytolytic T-cell effector functions and the role of CD4+ helper and regulatory T-cells[24,25]. The diverse mechanisms of CD4+ T-cell effector functions and their therapeutic potential received much less attention and remained incompletely understood[26–32]. In our work, we directly compare the anti-tumour effector functions of CD4+ and CD8+ T-cells. Using intravital microscopy, we demonstrate that CD4+ and CD8+ effector T-cells differ fundamentally in their mode and their site of action. We show how CD4+ effector T-cells operate at the tumour invasive margin, where they engage with recruited monocytes and initiate an indirect inflammatory killing process that depends on the release IFNγ and nitric oxide. Thereby, they eliminate MHC-deficient and IFN-unresponsive tumour cells that otherwise escape cytolytic CD8+ T-cell-mediated control. Finally, we have established a combinatorial therapeutic strategy that provides a framework for unleashing the full potential of CD4+ T-cell-mediated tumour immunity.

Eradication of immune evasive tumours

To better understand CD4+ T-cell effector functions in tumour tissues, we expanded on our previous experimental work using an adoptive cell transfer (ACT) of CD8+ T-cells in a mouse melanoma model[33]. As a source for tumour-specific T-cells, we employed pmel-1 TCRtg CD8+ T-cells and TRP-1 TCRtg CD4+ T-cells. Pmel-1 TCRtg CD8+ T-cells recognise a MHC-I binding peptide epitope of the melanocytic antigen Pmel/gp100 while TRP-1 TCRtg CD4+ T-cells recognise a MHC-II binding peptide epitope of the melanocytic antigen TRP-1[34,35]. To directly compare effector functions of adoptively transferred CD8+ and CD4+ T-cells under identical experimental conditions, we designed a recombinant adenovirus Ad-PT encoding a fusion protein of Pmel/gp100 and TRP-1 that includes both peptide epitopes recognised by the TCRtg T-cells (Fig. 1a). Our established ACT therapy protocol combines chemotherapeutic preconditioning with cyclophosphamide (C) one day prior to vaccination with recombinant adenovirus (V) and intravenous injections of TCRtg T-cells (T) followed by intratumoural injections of the immunostimulatory nucleic acids polyI:C and CpG as adjuvants (I) (Fig. 1b). This protocol was deliberately designed to activate both the adaptive and the innate arm of immune defence in a context that imitates an acute viral infection[36]. Initial experiments confirmed that Ad-PT was able to simultaneously activate adoptively transferred pmel-1 CD8+ and TRP-1 CD4+ T-cells (Extended Data Fig. 1a, b). However, the numbers of TRP-1 CD4+ T-cells present in peripheral blood were significantly lower when compared to pmel-1 CD8+ T-cells. Using ovalbumin as a model antigen, we also observed significantly lower numbers of adoptively transferred OT-II TCRtg CD4+ T-cells in peripheral blood when

compared to OT-I TCRtg CD8+ T-cells (Extended Data Fig. 1c, d), confirming the known intrinsic difference between CD4+ and CD8+ T-cells in relation to the proliferative capacity of these lymphocytes[37]. Nevertheless, adoptively transferred TRP-1 CD4+ T-cells were able to eradicate established B16 melanomas as efficiently as pmel-1 CD8+ T-cells (Fig. 1b, c; Extended Data Fig. 1e, f).

Next, we investigated whether TRP-1 CD4+ T-cells are able to control melanomas that lack MHC-I-deficient or IFN-unresponsive melanomas that are known to escape recognition and destruction by CD8+ T-cells[4,5]. We used HCmel12 mouse melanoma cells that can be readily genetically modified using CRISPR/Cas9 gene editing[38]. HCmel12 melanoma cells do not constitutively express MHC-I molecules, but strongly upregulate expression following exposure to IFNγ similar to B16 melanoma cells (Extended Data Fig. 1e, g). Accordingly, disruption of the genes encoding the MHC-I molecules H2-Kb and H2-Db or the IFN signalling molecule Jak1 both abrogated MHC-I expression on the surface of HCmel12 melanoma cells (Extended Data Fig. 1g). Robust growth of MHC-I-deficient tumours *in vivo* required antibody-mediated depletion of NK cells prior to tumour inoculation. Adoptively transferred TRP-1 CD4+ T-cells were able to eradicate genetically MHC-I-deficient as well as IFN-unresponsive HCmel12 cell variants that were not controlled by adoptively transferred pmel-1 CD8+ T-cells (Fig. 1d-f, Extended Data Fig. 1h). In addition, antibody-mediated depletion experiments confirmed that TRP-1 CD4+ T-cells can exert their anti-tumour effector functions independently of CD8+ T-cells (Extended Data Fig. 1i).

TRP-1 CD4+ T-cells were previously shown to eradicate B16 melanoma cells through direct recognition and cytotoxic destruction[30]. Since MHC-II molecules are not consistently expressed on human melanoma cells (Extended Data Fig. 2a)[11], we asked whether the presentation of peptide epitopes by MHC-II molecules on tumour cell surfaces is necessary for effective anti-tumour immunity. CRISPR/Cas9-mediated disruption of the *Ciita* gene coding for the MHC-II transactivator abrogated IFNγ-induced expression of MHC-II molecules on the surface of HCmel12 cells (Extended Data Fig. 2b). To verify antigen-specific recognition, we also generated HCmel12 cells that lack expression of the target antigen TRP-1 (Extended Data Fig. 2c). *In vitro* experiments confirmed that TRP-1 CD4+ T-cells directly recognise MHC-II-expressing HCmel12 cells in an antigen-specific manner (Fig. 1g). TRP-1 CD4+ T-cells are even more efficiently activated by dendritic cells pulsed with HCmel12 cells tumour lysates (Fig. 1h). Subsequent *in vivo* experiments demonstrated that TRP-1 CD4+ T-cells were able to eradicate established MHC-II-deficient, but not TRP-1-deficient HCmel12 melanomas (Fig. 1i, j, Extended Data Fig. 2d-g). Thus, TRP-1 CD4+ T-cells can exert anti-tumour activity through indirect antigen recognition on MHC-II+ tumour-infiltrating antigen-presenting cells.

Intratumoural CD4+ T-cell dynamics

MHC-II-expressing cells are consistently found in the tumour stroma (Extended Data Fig. 2a). We therefore hypothesised that the ability of CD4+ effector T-cells to efficiently interact with antigen-presenting cells might lead to a different spatial distribution and migratory behaviour in tumour tissues when compared to CD8+ T-cells. To address this hypothesis, we generated amelanotic (Tyr-KO) tagBFP-expressing HCmel12 cells, eGFP-expressing TRP-1 CD4+ T-cells and Venus-expressing pmel-1 CD8+ T-cells and performed *in vivo* fluorescence microscopy following ACT therapy (Extended Data Fig. 3a-b). Confocal microscopy of established amelanotic tagBFP-labelled HCmel12 tumours treated with adoptively transferred, eGFP+ TRP-1 CD4+ T-cells and Venus+ pmel-1 CD8+ T-cells revealed only very few CD4+ T-cells in tumour tissues when compared to CD8+ T-cells (Extended Data Fig. 3d-f), consistent with our observations in peripheral blood (Extended Data Fig. 1b). CD4+ T-cells were mostly found in local clusters at the invasive margin and only very rarely within the tumour centre, while CD8+ T-cells were abundant throughout the tumour tissue (Extended Data Fig. 3d-f). Intravital 2-photon microscopy confirmed the differential intratumoural localisation of adoptively transferred CD4+ and CD8+ T-cells and revealed substantial differences in their migratory behaviour (Fig. 2a-c, Extended Data Fig. 3g-l). Importantly, CD4+ T-cells arrested both in the stromal as well as in the tumoural compartment of the invasive margin, while CD8+ T-cells were highly motile in the stromal compartment and mainly arrested in association with tumour cells (Fig. 1b, c; Extended Data. Fig 3h,i; Supplementary Videos 1,2). These observations could be due to a preferential interaction of CD4+ T-cells with antigen-presenting cells within the stromal compartment of the invasive tumour margin *in vivo*.

A likely interaction partner for CD4+ T-cells are dendritic cells due to their ability to efficiently ingest and process tumour antigens for MHC-II-dependent antigen presentation[8,39,40]. To visualise antigen-specific interactions between TRP-1 CD4+ T-cells and dendritic cells, we additionally generated TRP-1-deficient amelanotic (TRP-1-KO and Tyr-KO) tagBFP-expressing HCmel12 cells (Extended Data Fig. 4a). TRP-

1-WT and TRP-1-KO tagBFP+ HCmel12 cells were injected into opposite legs of CD11c-Venus transgenic mice that harbour fluorescent dendritic cells[41] and treated with adoptively transferred eGFP+ TRP-1 CD4+ T-cells (Fig. 2d, Extended Data Fig. 4a). Confocal microscopy of established tumours revealed local accumulations of eGFP+ TRP-1 CD4+ T-cells in association with MHC-II-expressing Venus+ myeloid cells within tumour invasive margins only in TRP-1-WT but not in TRP-1-KO tumours (Fig. 2e, Extended Data Fig. 4c-e). In addition, surrounding tumour cells upregulated the expression of MHC-II only in TRP-1-WT mice, consistent with the notion that CD4+ T-cells were activated and locally secreted IFNγ. Importantly, intravital 2-photon microscopy demonstrated that CD4+ T-cells arrested and showed long-lasting close interactions between eGFP+ TRP-1 CD4+ T-cells and Venus+ myeloid cells only in TRP-1-WT but not in TRP-1-KO tumours (Fig. 2f, g, Extended Data Fig. 4f, g; Supplementary Video 3). Taken together, our findings indicate that TRP-1 CD4+ effector T-cells locally cluster with MHC-II-expressing CD11c+ myeloid cells at the tumour invasive margin where they maintain prolonged antigen-specific interactions leading to the local secretion of IFNγ *in vivo*.

Recruitment of IFN-activated monocytes

To better understand how a comparatively small number of CD4+ effector T-cells cause the eradication of established tumours, we profiled treatment-induced alterations of the tumour immune microenvironment by flow cytometry (Extended Data Fig. 5a). Initial experiments in CD11c-Venus mice revealed that a substantial subset Venus+ MHC-II+ cells in CD4 ACT-treated tumours also expressed CCR2 and high levels of Ly6C. This suggested that among the CD11c-Venus+ cells bona fide dendritic cells were replaced by Venus+ MHC-II+ inflammatory monocytes in response to therapy (Fig. 3a). Treated tumours in CD11c-Venus mice indeed showed a strong increase of all inflammatory monocytes, many of which expressed CD11c-Venus (Extended Data Fig. 5a, b). A comprehensive characterisation of tumour-infiltrating myeloid cells in wild type mice over time confirmed the dynamic recruitment of inflammatory CD11b+CCR2+Ly6C-hi monocytes with a peak at day 5 after CD4+ T-cell transfer, while the number of CD11c+MHC-II+F4/80- conventional and of SiglecH+Sirp1a+ plasmacytoid dendritic cell declined (Fig. 3b, Extended Data Fig. 5c). At the same time, adoptively transferred TRP-1 CD4+ T-cells dynamically accumulated in tumour tissues (Extended Data Fig. 5d). A compilation of all tumour-infiltrating immune cells demonstrates that our CD4 ACT regimen dynamically modified the tumour immune microenvironment with a particular shift towards a myeloid-dominated immune compartment (Extended Data Fig. 5e).

Our ACT treatment protocol combined the *in vivo* activation of CD4+ T-cell effector functions with additional innate immune stimulation using polyI:C and CpG. To separate the contribution of both interventions for the recruitment and activation of monocytes, we omitted either the innate stimuli or the CD4+ T-cell transfer from our combined ACT therapy scheme and performed single-cell RNA-seq analyses of sorted CD11b+ Ly6G- tumour-infiltrating immune cells (Extended Data Fig. 6a; Fig. 3c, d). Dimensionality reduction and visualisation using UMAP showed a separate clustering of myeloid cells between untreated and all treated conditions with most pronounced effects occurring after combined activation of innate and adaptive immunity (Extended Data Fig. 6b; Fig. 3e). Automated cell type assignment using singleR classified the vast majority of cells in all treated groups (>80%) as monocytes (Extended Data Fig. 6c; Fig. 3f), confirming flow cytometric observations (Extended Data Fig. 5e). Differential gene expression and gene set enrichment analyses between myeloid cells from untreated and CD4 ACT treated tumours revealed a strong activation of IFN-response genes upon therapy (Extended Data Fig. 6d, e). Importantly, both innate immune stimulation and CD4+ effector T-cells independently induced the expression of IFN-response genes (Extended Data Fig. 6e; Fig. 3g). Unsupervised Leiden clustering for untreated and CD4 ACT-treated groups dissected 4 and 7 cell states, respectively (Fig. 3h). Pseudotime inference and subsequent graph abstraction using PAGA identified three distinct trajectories in CD4 ACT-treated mice, corresponding to differentiation pathways towards phenotypes of monocyte-derived dendritic cells (ACT1), monocyte-macrophage effectors (ACT2a-c) and Ly6c-Lo mature monocytes (ACT3a,b), as indicated by the expression of a selected panel of characteristic marker genes (Extended Data Fig. 6g; Fig. 3i, j). The endpoint cellular states of these three trajectories in CD4 ACT-treated mice represent IFN-activated counterparts of the intratumoural monocyte-macrophage network found in untreated controls (NT1-NT3). Taken together, the flow cytometric and transcriptomic analyses reveal that CD4+ T-cells and innate immune stimuli synergistically initiate a self-amplifying loop that reprogrammed the myeloid network in treated tumours. This network is characterised by the recruitment of inflammatory monocytes which acquire IFN-activated cellular states and dynamically shift towards MHC-II antigen-presenting and potentially tumouricidal effector phenotypes.

Inflammatory tumour cell killing

Our data show that CD4+ effector T-cells and innate immune stimulation independently promoted the recruitment of IFN-activated inflammatory monocytes into the tumour microenvironment. Next, we asked whether CD4+ T-cells and innate immune stimuli synergised on a quantitative or on a qualitative level for the acquisition of tumouricidal monocyte effector functions. The absolute numbers of inflammatory Ly6C-hi monocytes in the tumour were not significantly altered when innate stimuli were omitted from our combined ACT therapy regimen (Fig. 4a). By contrast, both CD4+ T-cells and innate immune stimulation were indispensable for full iNOS induction in the recruited monocytes (Fig. 4b, Extended Data Fig. 7a). Functionally, the synergism of the combined therapy was required for the eradication of established tumours leading to a striking increase in tumour-free survival (Fig. 4c, Extended Data Fig. 7b). We hypothesised that the release of IFNγ was responsible for the CD4+ T-cell-driven qualitative enhancement of tumouricidal monocyte effector functions on the molecular level. In agreement with our previous results (Fig. 4a, b, Extended Data Fig. 7a), antibody-mediated neutralisation of IFNγ did not influence the absolute number of tumour-infiltrating monocytes, but significantly reduced the frequency of iNOS-expressing monocytes (Fig. 4d, e, ED Fig. 7c). Importantly, CD4 T-cell-derived IFNγ was essential to eradicate established tumours (Fig. 4f, Extended Data Fig. 7d).

CD4+ T-cell-derived IFNγ can either act directly on tumour cells or indirectly through IFN-dependent activation of myeloid cells and the production of nitric oxide[22,26,31,42]. We hypothesised that nitric oxide produced by iNOS-expressing myeloid cells would be of particular importance for efficient indirect killing of IFN-unresponsive and MHC-deficient melanoma cells. To address this hypothesis, we investigated the impact of a highly specific iNOS inhibitor (N6-(1-iminoethyl)-L-lysine, L-NIL) on CD4 ACT treatment responses of established Jak1-KO tumours in direct comparison to Ciita-KO HCmel12 tumours. Jak1-KO HCmel12 cells are genetically IFN-unresponsive (Extended Data Fig. 1g) and as a consequence of disrupted IFN signalling are also functionally deficient not only for MHC-I but also for MHC-II expression (Extended Data Fig. 8a). In contrast, Ciita-KO HCmel12 cells are genetically MHC-II deficient (Extended Data Fig. 2b) but IFN-responsive as evidenced by IFNγ-dependent upregulation of MHC-I expression (Extended Data Fig. 8a). In support of our hypothesis, iNOS activity was essential for indirect destruction of IFN-unresponsive Jak1-KO tumours but was not specifically required for the control of IFN-responsive Ciita-KO tumours by CD4+ effector T-cells (Fig. 4g, h, Extended Data Fig. 8b, c). Together, our results provided evidence that CD4+ effector T-cells indirectly kill IFN-unresponsive, MHC-deficient tumour cells *in vivo* through IFN-dependent activation of myeloid effector cells and the production of nitric oxide.

CD4+ T-cell-derived IFNγ has previously been shown to act directly on IFN-responsive tumour cells and to induce cellular senescence[32]. Our results raised the question how myeloid cell-derived nitric oxide contributes to the killing of tumour cells that are IFN-unresponsive. Recent data that elucidated the cytokine driven immunopathology in COVID-19 patients revealed an inflammatory mode of apoptotic cell death driven by the concerted action of IFNγ, TNF, and nitric oxide[43]. Inspired by these observations, we hypothesised that these inflammatory mediators were also involved in killing melanoma cells in the course of our CD4 ACT treatment. Therefore. we studied the impact of the nitric oxide donor S-nitroso-N-acetylpenicillamine (SNAP) and of the inflammatory cytokine IFNγ on TNF-mediated melanoma cell death *in vitro* (Fig 4i, Extended Data Fig. 9a). Neither TNF nor IFNγ alone induced substantial apoptotic cell death in IFN-unresponsive Jak1-KO or in IFN-responsive Ciita-KO HCmel12 cells. The combination of TNF and IFNγ also did not affect the survival of Jak1-KO HCmel12 cells but dramatically increased cell death in Ciita-KO cells, indicating that activation of the IFN-signaling cascade can sensitise IFN-responsive cells for TNF-induced apoptosis. Importantly, the nitric oxide donor SNAP strongly induced cell death in Jak1-KO HCmel12 cells even without TNF, while SNAP-induced cell death of IFN-responsive Ciita-KO cells was enhanced in combination with TNF (Fig 4j, Extended Data Fig. 9b). Of note, the ability of these inflammatory mediators to act in concert and induce apoptotic cell death was fully recapitulated in a panel of IFN-responsive and IFN-unresponsive human melanoma cell lines (Fig 4k, Extended Data Fig. 9c). These *in vitro* results demonstrate that myeloid cell-derived nitric oxide is particularly effective in promoting apoptotic cell death of IFN-unresponsive melanoma cells. Thereby, nitric oxide complements the ability of IFNγ to sensitise IFN-responsive melanoma cells towards TNF-induced cell death.

Discussion

For many years, CD4+ T-cells have primarily been thought to act as helper cells for the activation of CD8+ effector T-cells[24], which kill tumour cells by direct cytolysis. Recently, evidence has accumulated that CD4+ T-cells can also exert direct cytolytic effects against MHC-II-expressing tumour cells. However, during tumour evolution, malignant cells escape direct T-cell recognition through genetic loss or downregulation of MHC expression[44]. Our results highlight the ability of CD4+ T-cells to cooperate

with myeloid cells and eliminate tumour cells independent of direct recognition that was first observed in experiments inspired by investigations to understand immune resistance of mice to bacterial pathogens[19 20]. We faithfully recapitulate in our experimental model the previously described cellular and molecular mechanisms underlying this cooperation, many of which are shared between immune responses to tumours and pathogens. Specifically, indirect antigen presentation, IFN-dependent recruitment of mononuclear phagocytes and killing at a distance through inflammatory mediators critically contribute to the control tumours[22,28,45] and pathogens[46,47] alike. In our work we directly demonstrate that this mode of action allows CD4+ T-cells to control MHC-deficient as well as IFN-unresponsive tumour cell variants that evade direct T-cell recognition and cytolytic killing. This complements recent observations demonstrating that an interaction between CD4+ T-cells and NK cells can also control tumours that evade CD8+ T-cell control[48].

Importantly, our experimental model enabled us to dissect the *in vivo* dynamics and the critical interaction partners for CD4+ effector T-cells in tumour tissues in direct side-by-side comparison to cytotoxic CD8+ effector T-cells. Our results show that the dynamics and function of CD4+ T-cells follow fundamentally different rules than their CD8+ counterparts. Specifically, we found that only very few CD4+ T-cells infiltrated tumour tissues where they preferentially cluster at the invasive margin of tumours and engage in antigen-dependent interactions with CD11c+MHC-II+ myeloid cells. By contrast, large numbers of CD8+ T-cells briskly infiltrated deep into tumour tissues. The strategic positioning of CD4+ T-cells at the tumour invasive margins allowed them to effectively drive the recruitment of an increasing number of IFN-activated monocytes into the tumour microenvironment. Despite their low abundance, CD4+ T-cells modulated the phenotypic development of incoming monocytes along differentiation paths towards antigen-presenting and tumouricidal effector phenotypes. This initiates a self-amplifying loop that reprogrammes the myeloid network in the tumour microenvironment. Additional innate immune stimulation boosted tumouricidal effector functions of monocytes and enabled tumour regression from the outside (Extended Data Fig. 10). Together, our data demonstrate that CD4+ effector T-cells preferentially recognise and kill tumour cells indirectly in cooperation with myeloid cells, reminiscent of immune-mediated control of certain pathogens for which antigen presentation and IFN-mediated control also relies exclusively on indirect mechanisms.

Our work also provides insights into the dynamic development of the monocyte-dendritic cell-macrophage lineage under inflammatory conditions[49,50]. In particular, we show how CD4+ T-cells can rapidly recruit monocyte precursors into tumour tissues and direct their differentiation towards antigen-presenting and effector phenotypes. A similar phenotypic plasticity of monocytes under inflammatory conditions has recently been reported in models of viral infection[51], supporting the notion of shared mechanisms of immune protection against tumours and pathogens.

Further dissecting the critical molecular determinants of our therapeutic approach, we found that IFNγ-induced nitric oxide production by myeloid cells was essential for indirect recognition and destruction of IFN-unresponsive and MHC-deficient tumours. Subsequent *in vitro* investigations showed that nitric oxide promoted apoptotic cell death of IFN-unresponsive melanoma cells, complementing the ability of IFNγ to sensitise IFN-responsive melanoma cells for TNF-induced cytotoxicity. These observations reconcile seemingly contradictory reports regarding the role of IFNγ and nitric oxide in different experimental models[26,32]. Apoptotic cell death due to dynamic local accumulation of IFNγ and nitric oxide can also be observed in infected tissues and likely represents an important component of the shared disease-agnostic inflammatory defence mechanism[52]. This notion is supported by the recent report that immunopathology during acute SARS-CoV-2 infections results from wide-spread inflammatory cell death due to aberrantly increased systemic levels of IFNγ and TNF[43].

Taken together, our experimental investigations provide a comprehensive picture of the spatial organisation and the dynamics of T-cell effector functions in tumour tissues. Our results emphasise the ability of CD4+ effector T-cells to indirectly recognise and kill tumour cells independent of their MHC expression and their IFN responsiveness. CD4+ effector T-cells and stimulation of innate pathogen recognition receptors together reprogram the myeloid network in the tumour microenvironment and orchestrate an inflammatory mode of apoptotic tumour cell death that is initiated at the invasive margins. This indirect “outside-in” killing complements direct MHC-dependent recognition and cytolytic destruction of tumour cells and controls tumour immune evasion. Our work suggests a great potential for new treatment options that target CD4+ effector T-cells and simultaneously activate non-specific innate inflammatory defence mechanism active against tumours and pathogens. This opens new avenues of research to advance cancer immunotherapies.

Methods

Mice

Wild type C57BL/6J mice were purchased from Janvier or Charles River. The T cell receptor-transgenic pmel-1 (B6.Cg-Thy1a/Cy Tg(TcraTcrb)8Rest/J) and TRP-1 (B6.Cg-Rag1tm1Mom Tyrp1B-w Tg(Tcra,Tcrb)9Rest/J) mice, the fluorescent B6-eGFP (C57BL/6-Tg(UBC-GFP)30Scha/J) and CD11c-eYFP (B6.Cg-Tg(Itgax-Venus)1Mnz) mice, and the congenic CD45.1 (B6.SJL-*Ptprc*^{a}*Pepc*^{b}/Boy) mice were purchased from Jackson Laboratories. Pmel-1-Venus mice were generated by crossing CAG-Venus mice with pmel-1 mice. TRP-1-eGFP mice were generated by crossing B6-eGFP mice into the TRP-1-deficient Rag-KO background of TRP-1 mice. All transgenic mice were bred in house. Age matched cohorts of tumour developing mice were randomly allocated to the different experimental groups. All animal experiments were conducted with male mice on the C57BL/6 background under specific pathogen-free conditions in individually ventilated cages according to the institutional and national guidelines for the care and use of laboratory animals with approval by the Ethics Committee of the Office for Veterinary Affairs of the State of Saxony-Anhalt, Germany (permit license numbers 42502-2-1393 Uni MD, 42502-2-1586 Uni MD, 42502-2-1615 Uni MD) in accordance with legislation of both the European Union (Council Directive 499 2010/63/EU) and the Federal Republic of Germany (according to § 8, Section 1 TierSchG, and TierSchVersV).

Cell lines and cell culture

The mouse melanoma cell line HCmel12 was established from a primary melanoma in the Hgf-Cd4k^{R24C} mouse model by serial transplantation in our laboratory as described previously[53]. The mouse melanoma cell line B16 and the human melanoma cell lines A375 and SKmel28 were purchased from ATCC (Manassas, VA, USA). The human melanoma cell lines MaMel04 and MaMel102 were kindly provided by Dirk Schadendorf. All cell lines were cultured in “complete RPMI medium” consisting of RPMI 1640 medium (Life Technologies) supplemented with 10% FCS (Biochrome), 2 mM L-Glutamine, 10 mM non-essential amino acids, 1 mM HEPES (all form Life Technologies), 20 µM 2-mercoptoethanol (Sigma), 100 IU/ml penicillin and 100 µg/ml streptomycin (Invitrogen) in a humidified incubator with 5% CO_2. The cell lines were routinely screened for mycoplasma contamination.

Adenovirus generation and expansion

To generate the adenoviral vaccine Ad-PT, a fusion construct was generated consisting of the first 150 base pairs of the human *PMEL* cDNA (coding for aa1-50 of the human PMEL/gp100 protein including the CD8+ T cell epitope KVPRNQDWL) and 1404 base pairs of the mouse *Trp1* cDNA (coding for aa51-518 including the CD4+ T cell epitope SGHNCGTCRPGWRGAACNQKILTVR) followed by sequences coding for a T2A viral self-cleaving peptide and the fluorescent marker protein eYFP. This vaccine construct was cloned into the pShuttle vector (termed pShuttle-PT-YFP). A recombinant adenovirus vector with this sequence was then generated by a recombineering technique in *E. coli* strain SW102 using bacmid pAdZ5-CV5-E3+. The E1 region of this bacmid is replaced by a selection/counter-selection cassette called Ampicillin, LacZ, SacB (ALS cassette). Next, *E. coli* with this bacmid were electroporated with the PT-YFP transgene with homology arms flanking the ALS cassette obtained by PCR amplification using pShuttle-PT-YFP as a template. Positive colonies were isolated after antibiotic selection on LB-sucrose plates. SacB enzyme toxin uses sucrose as a substrate for a toxin and thus sucrose inhibits the growth of negative colonies with the intact ALS cassette. Ad-PT and Ad-OVA were expanded utilising the 911 human embryonic retinoblast cell line. A confluent monolayer of the cells in T175 cell culture flasks was infected with Ad-PT at MOI 1. The cytopathic effects were observed at around 36 hours of incubation at 37°C. Then, cells were scraped, freeze-thawed three times and the lysates were cleared by centrifuging at the speed of 7000 x g for 45 minutes. The crude virus was then titrated by the $TCID_{50}$ method according to standard protocols.

CRISPR-Cas9 cell engineering

To generate *Jak1*-KO, *MHC-I*-KO (H2-Db and H2-Kb double knockout), *Ciita*-KO, *Trp1*-KO and *Tyr*-KO HCmel12 variants, wild-type HCmel12 melanoma cells were seeded into a 12-well plate at a density of $5x10^5$ cells per well. The cells were co-transfected with 1.6 µg pX330-sgRNA and 0.4 µg plasmid expressing green fluorescent protein (pRp-GFP) using Fugene HD transfection reagent (Promega) according to manufacturer’s instructions. GFP positive cells were single cell sorted using a FACSAria III Cell Sorter (BD) to generate polyclonal and 3-4 monoclonal populations per targeted gene. The frequency of specific out-of-frame mutations was analysed by next-generation sequencing (Illumina MiSeq platform). HCmel12 cells were mock transfected with pX330 plasmid without sgRNA and the polyclonal cell line was used as a CRISPR-control in all performed experiments. Genomic DNA from

cultured knockout variants was extracted using the NucleoSpin Tissue kit (Macherey-Nagel) according to the manufacturer's protocol. A two-step PCR protocol was performed to generate targeted PCR amplicons for next-generation sequencing. In the first PCR, specific primers for the target gene with additional adapter sequences complementary to the barcoding primers were used to amplify the genomic region of interest with Phusion HD polymerase (New England Biolabs). In a second PCR, adapter-specific universal primers containing barcode sequences and the Illumina adapter sequences P5 and P7 were used (Illumina barcodes: D501-508 & D701-D712). Next-generation sequencing was performed with MiSeq Gene & Small Genome Sequencer (Illumina) according to manufacturer's standard protocols with a single-end read and 300 cycles (MiSeq Reagent Kit v2 300 cycle). For the detection of insertions or deletions, the web-based program Outknocker (http://www.outknocker.org/) was used as previously described[54]. FASTQ files were imported, and the sequence of the target gene amplicons was used as reference sequence for alignment.

Tumour transplantation experiments

For tumour inoculation, a total of 2 x 10^5 cells were injected intracutaneously into the shaved flanks or hindlegs of mice with a 30G (0.3 x 13 mm) injection needle (BD). Tumour development was monitored by inspection and palpation. Tumour sizes were measured 3 times weekly using callipers and presented as the mean of the two largest perpendicular diameters. Mice were sacrificed when tumours exceeded 10-15 mm in mean diameter. All experiments were performed in groups of four to six mice and repeated independently at least twice.

Adoptive cell transfer (ACT) therapy protocol

ACT therapy was performed as previously described[36]. In brief, when transplanted melanoma cell lines reached a mean diameter of 3 to 5 mm, mice were preconditioned for ACT by a single i.p. injection of 2 mg (100 mg/kg) cyclophosphamide in 100 µl PBS one day before intravenous delivery of 2 x 10^6 naïve gp100-specific $CD8^+$ pmel-1 T cells and/or 0.5 x 10^6 naïve TRP-1-specific $CD4^+$ T cells (in 100 µl PBS), isolated from spleens of TCR-transgenic pmel-1 and/or TRP-1 donor mice. The adoptively transferred T cells were activated *in vivo* by a single i.p. injection of 2.5 x 10^8 PFU of the recombinant adenoviral vaccine Ad5-PT in 100 µl PBS. 50 µg of CpG 1826 (MWG Biotech) and 50 µg of polyinosinic:polycytidylic acid (polyI:C, Invivogen), diluted in 100 µl distilled water, were injected intratumourally 3, 6 and 9 days after T cell transfer. Seven days after T cell transfer, blood was taken routinely from the *Vena facialis* to confirm successful expansion of transferred T cells via flow cytometry.

Supplementary in vivo treatments

NK cell depletion was performed by a single i.p. injection of 200 µg anti-NK1.1 antibody (clone PK136, BioXCell) in 100 µl, diluted in pH 7.0 Dilution Buffer (BioXCell). CD8+ T cell depletion was performed by i.p. injections of initially 100 µg, followed by weekly injections of 50 µg anti-CD8 antibody (clone 2.43, BioXCell). IFNg-blockade was performed by weekly i.p. injection of 500 µg anti-IFNg antibody (clone XMG1.2, BioXCell) in 100 µl, diluted in pH 8.0 buffer. Inhibition of iNOS was performed by daily i.p. injection of 200 µg N6-(1-iminoethyl)-L-lysine, dihydrochloride (L-NIL, Cayman Chemicals), diluted in 100 µl phosphate-buffered saline.

Flow cytometry

Immunostaining of single cell suspensions was performed according to standard protocols. Single suspensions were incubated with anti-CD16/CD32 (clone 93; Biolegend) before staining with fluorochrome-conjugated monoclonal antibodies. Intracellular staining was carried out using a Fixation/Permeabilization Solution Kit (BD or Biolegend). Single cell suspensions from tumours were first stained with antibodies against cell-surface antigens, then fixed and permeabilized followed by intracellular staining. Dead cell exclusion was performed using 7-Aminoactinomycin (7-AAD), propidium iodide (PI) or Zombie NIR fixable viability dye (Biolegend). All data were acquired with an Attune NxT acoustic focusing flow cytometer (ThermoFisher) and analysed using FlowJo v10 software for Windows (Tree Star, Inc.). Fluorescence-activated cell sorting (FACS) was performed with an Aria III (BD Biosciences).

Analysis of tumour cell MHC expression and antigen recognition by CD4+ T cells

To quantify the expression of MHC molecules, tumour cells were pre-treated with 100 U/ml recombinant murine IFNg (Prepotech) for 72h and then analysed by flow cytometry. To assess antigen-recognition by CD4+ T cells, TRP-1 TCRtg mice were immunised with Ad-PT and subsequently injected with 50 µg

CpG and 50 µg polyI:C intracutaneously 3 and 6 days after immunisation. TRP-1 CD4+ T cells were isolated from the spleen and purified by two rounds of magnetic cell sorting (Miltenyi). Direct antigen recognition was determined by co-culturing purified CD4+ T cells with IFNg pre-treated HCmel12 cells. Indirect antigen recognition was assessed by initially generating bone marrow-derived dendritic cells with recombinant GM-CSF and IL-4 (Peprotech) as previously described. After one week, differentiated bone marrow-derived dendritic cells were then pulsed overnight with HCmel12 lysate, prior to co-culture with purified CD4+ T cells. For both direct and indirect antigen recognition assays, the production of IFNg from the CD4+ T cells was measured 16h after co-culture by intracellular cytokine staining using flow cytometry.

Calculations of absolute immune cell counts in tumour tissues

Tumours were excised with tweezers and scissors and weighed using the Entris 224-1S analytical balance (Sartorius). Single cell suspensions were created mechanically using 5 ml syringe plungers (BD) and 70 µm cell strainers (Greiner). After immunostaining, cells were resuspended in a defined volume and analysed on the Attune NxT acoustic focusing flow cytometer that uses a unique volumetric sample and sheath fluid delivery system allowing for accurate measurements of the volumes of acquired samples, and thus accurate calculation of cell concentrations. Absolute cell counts were calculated using the following equation: Absolute cell count (cells per mg) = Recorded cell count/tumour weight (mg)/recorded proportion of total cell suspension volume (decimal value).

Immunofluorescence microscopy

Tumours were harvested on day 5 after adoptive TCRtg T cells and fixed in 4% paraformaldehyde for 24 hours, then dehydrated in 20% sucrose prior to embedding in OCT freezing media (Sakura Finetek). Next, 6 µm sections were cut on a CM305S cryostat (Leica), adhered to Superfrost Plus slides (VWR) and stored at -20°C until further use. When thawed, slides were either fixed with ice-cold acetone and stained with indicated antibodies or directly mounted with Vectashield Antifade Mounting Medium (Vector Laboratories). Images were acquired on an Axio Imager.M2 with a Colibri 7 LED illumination system (Zeiss) and analysed with ImageJ (http://imageJ.nij.gov/ij).

Intravital 2-photon microscopy

Mice were anaesthetised with 100 mg/kg ketamine and 10 mg/kg xylazine i.p., complemented by 3 mg/kg acepromazine s.c. after the onset of anaesthesia. The animals were placed and fixed to a heated stage. Transparent Vidisic® carbomer gel was applied to moisture the eyes during anaesthesia. The hind leg was fixed in an elevated position and the skin covering the melanoma was detached using surgical scissors and forceps. One drop of transparent Vidisic® carbomer gel was used on the exposed site as mounting medium. Two component STD putty (3M ESPE) placed on both sides of the leg was used create a level surface using a 24 x 60 mm cover slip which was gently pressed on the putty in a way that the coverslip made slight contact with the exposed site without exerting pressure on the tumour. After complete polymerisation of the putty, the mice were transferred onto a 37° C heating plate under the 2-photon microscope.

Imaging was performed using distilled water or transparent Vidisic® carbomer gel as immersion liquid with a W Plan-Apochromat 20x/1,0 DIC VIS-IR objective mounted to a Zeiss LSM 700 upright microscope with the ZEN software environment (Version 2.1, Zeiss), or a LaVision TrimScope mounted to an Olympus BX50WI fluorescence microscope stand and a XLUMPlanFI 20/0.95 objective. Excitation on the LSM700 setup was performed with Mai Tai DeepSee (tuned to 800 nm) and Insight X3 (tuned to 980 nm) Ti:Sa oscillators (both from Spectra-Physics), Venus, SHG, tagBFP and eGFP fluorescence were read out on a detector cascade with 520 nm dichroic with 534/30 nm BP (transmitted, 980 nm excitation), 445 nm dichroic (deflected, 800 nm excitation), and 490 nm dichroic with 485 nm SP for deflected (800 nm excitation) and 525/50 nm BP for transmitted fluorescence, respectively. Excitation on the TrimScope setup was performed with a Chamaeleon Ultra II TI:Sa oscillator tuned to 880 nm with a double split detector array with a 495 nm main dichroic and a 445 nm and 520 nm secondary dichroics for SHG, tagBFP filtered with a 494/20 BP, eGFP filtered with a 514/30 nm BP, and Venus filtered with a 542/27 nm BP filter, respectively. Non-descanned PMT (for SHG, Venus, and eGFP in the TrimScope Setup) and high sensitivity detectors (for tagBFP and eGFP in the Zeiss setup) were used for signal collection.

Typically, three to four representative field of views of 353 μm^2 size in x- and y- and a z-range of 48 to 60 µm with 4 µm step size were chosen for data acquisition. Z-stacks were captured in 30-60 second intervals and individual movie length was 15-30 minutes. Data analysis was performed with the Bitplane Imaris software (V8.3 to 9.7). T cells were identified using the Imaris spot function. Tumour area was

identified using the surface function with low surface detail. CD11c-Venus cells were identified using the surface function with high detail. T cell speed was calculated using the Imaris software. Cells were considered arrested when speed was < 2µm/min. Contact duration was measured as the time that the distance between the centre of mass of a T cell to the closest CD11c cell surface was < 8µm. Snapshot images of 3D rendering and tracking were cropped, arranged and animated for time series using Fiji (ImageJ Version 1.51 s, http://imageJ.nij.gov/ij).

Cell preparation for single-cell RNA sequencing

Tumours were harvested and processed into a single suspension. CD45+ cells were enriched using a positive selection kit (Miltenyi). Next, individual samples were hashtagged with unique TotalSeq-B hashtag antibodies B0301-B0310 (Biolegend) and subsequently stained with fluorescently labelled antibodies. Cell sorting of $1.2x10^5$ $CD45^+CD11b^+Ly6G^-$ cells was performed with an Aria III (BD) and loaded onto one lane of a 10x Chromium microfluidics controller. cDNA of hashtag and gene expression libraries were amplified, and indices added via PCR. Sequencing was performed on an Illumina Novaseq on two lanes of a S1 cartridge with 150 bp read length in paired end mode. Reading depth was calculated to obtain ~50.000 reads/cell for the gene expression library and 5.000 reads/cell for the hashtag library.

Single-cell RNA-seq data processing and hashtag-demultiplexing

The scRNA-seq data generated via 10X Genomics Chromium technology were aligned and quantified using the Cell Ranger Single-Cell Software Suite against the mm10 mouse reference genome. The raw, unfiltered data generated from Cell Ranger were used for downstream analysis. Quality control was performed on cells based on the three metrics: total UMI count, number of detected genes and proportion of mitochondrial gene count per cell. Specifically, cells with < 1000 UMIs, 1000 detected genes, and more than 25% mitochondrial UMIs were filtered out. To remove potential doublets, cells with UMI count above 40,000 were removed. Subsequently, we demultiplexed the samples tagged with distinct hashtag-oligonucleotides using Solo[55]. After quality control, we normalized raw counts by their size factors using scran[56] and subsequently performed log2 transformation. The logarithmised and normalised count matrix was used for the downstream analysis.

Dimension reduction, unsupervised clustering and differential gene expression analyses

Analysis of normalised data was performed using scanpy[57]. Initially, the 4000 most highly-variable genes were selected for subsequent analysis using scanpy.pp.highly_variable_genes with the parameter „n_top_genes=4000“. Next, a principal component analysis (PCA) was performed with 50 components using scanpy.tl.pca with the parameters „n_comps=50, use_highly_variable=True, svd_solver='arpack'“. Subsequently, dimensionality reduction was performed using Uniform Manifold Approximation and Projection (UMAP) with scanpy.tl.umap. Single cells were automatically assigned using SingleR[58], with transcriptomes from the Immunological Genome Project as a reference. Clustering of single cells by their expression profiles was conducted employing the Leiden-algorithm using scanpy.tl.leiden with the parameter „resolution=1.5“. Clusters with fewer than 20 cells were removed from further analysis. Differential gene expression was performed between cell classified as macrophages and monocytes from untreated and CD4 ACT treated mice using a hurdle model implemented in the R package “MAST”. Subsequent gene set enrichment analysis was performed using GSEA in preranked mode using the log2 fold change as ranking metric. The interferon score was derived by calculating a z-score for all genes from the MSigDB gene set “HALLMARK_INTERFERON_GAMMA_RESPONSE” for each cell.

RNA velocity

For RNA velocity, count matrices of spliced and unspliced RNA abundances were generated using the velocyto workflow for 10x chromium samples with the genome annotation file supplied by 10x Genomics for the mm10 genome and a repeat annotation file retrieved from the UCSC genome browser. Subsequent analyses were performed using scVelo[59]. The count matrices were loaded into the scanpy environment, merged with the previously generated anndata objects and normalized using scvelo.pp.filter_and_normalize. Next, moments for velocity estimation were calculated, gene-specific velocities were estimated, and the velocity graphs were computed. Furthermore, a partition-based graph abstraction graph was generated with velocity-directed edges.

In vitro cell death assays

For the measurements of apoptosis in murine and human melanoma cell lines cells were first seeded in 96-well plates in complete RPMI medium. Inflammatory mediators were added after 24h (10 U/ml recombinant murine IFNg (Peprotech); 1000 U/ml recombinant murine TNFa (Peprotech); 100 U/ml animal-free recombinant human IFNg (Peprotech); 1000 U/ml recombinant human TNFa (Peprotech) and 100 µM S-nitroso-N-acetylpenicillamine (SNAP, Cayman Chemicals). After 24 hours, floating and adherent cells where harvested and stained using the FITC Annexin V Apoptosis Detection Kit I (BD Pharmingen) and analysed using the Attune NxT acoustic focusing flow cytometer (ThermoFisher).

References

1. Tumeh, P. C. *et al.* PD-1 blockade induces responses by inhibiting adaptive immune resistance. *Nature* **515**, 568–571 (2014).
2. Chen, D. S. & Mellman, I. Elements of cancer immunity and the cancer–immune set point. *Nature* **541**, 321–330 (2017).
3. Waldman, A. D., Fritz, J. M. & Lenardo, M. J. A guide to cancer immunotherapy: from T cell basic science to clinical practice. *Nat. Rev. Immunol.* **20**, 651–668 (2020).
4. Khong, H. T. & Restifo, N. P. Natural selection of tumor variants in the generation of “tumor escape” phenotypes. *Nat. Immunol.* **3**, 7 (2002).
5. Keenan, T. E., Burke, K. P. & Van Allen, E. M. Genomic correlates of response to immune checkpoint blockade. *Nat. Med.* **25**, 389–402 (2019).
6. Haas, L. *et al.* Acquired resistance to anti-MAPK targeted therapy confers an immune-evasive tumor microenvironment and cross-resistance to immunotherapy in melanoma. *Nat. Cancer* **2**, 693–708 (2021).
7. Kreiter, S. *et al.* Mutant MHC class II epitopes drive therapeutic immune responses to cancer. *Nature* **520**, 692–696 (2015).
8. Binnewies, M. *et al.* Unleashing Type-2 Dendritic Cells to Drive Protective Antitumor CD4+ T Cell Immunity. *Cell* **177**, 556-571.e16 (2019).
9. Oh, D. Y. *et al.* Intratumoral CD4+ T Cells Mediate Anti-tumor Cytotoxicity in Human Bladder Cancer. *Cell* **181**, 1612-1625.e13 (2020).
10. Zheng, L. *et al.* Pan-cancer single-cell landscape of tumor-infiltrating T cells. *Science* **374**, abe6474 (2021).
11. Oliveira, G. *et al.* Landscape of helper and regulatory antitumour CD4+ T cells in melanoma. *Nature* (2022) doi:10.1038/s41586-022-04682-5.
12. Melenhorst, J. J. *et al.* Decade-long leukaemia remissions with persistence of CD4+ CAR T cells. *Nature* **602**, 503–509 (2022).
13. Rosenberg, S. A. & Restifo, N. P. Adoptive cell transfer as personalized immunotherapy for human cancer. *Science* **348**, 62–68 (2015).
14. Ribas, A. & Wolchok, J. D. Cancer immunotherapy using checkpoint blockade. *Science* **359**, 1350–1355 (2018).
15. Ahrends, T. & Borst, J. The opposing roles of CD4 $^{+}$ T cells in anti-tumour immunity. *Immunology* **154**, 582–592 (2018).
16. Veatch, J. R. *et al.* Tumor-infiltrating BRAFV600E-specific CD4+ T cells correlated with complete clinical response in melanoma. *J. Clin. Invest.* **128**, 1563–1568 (2018).
17. Śledzińska, A. *et al.* Regulatory T Cells Restrain Interleukin-2- and Blimp-1-Dependent Acquisition of Cytotoxic Function by CD4+ T Cells. *Immunity* **52**, 151-166.e6 (2020).
18. Oh, D. Y. & Fong, L. Cytotoxic CD4+ T cells in cancer: Expanding the immune effector toolbox. *Immunity* **54**, 2701–2711 (2021).
19. Evans, R. & Alexander, P. Cooperation of immune lymphoid cells with macrophages in tumour immunity. *Nature* **228**, 620–622 (1970).
20. Mackaness, G. B. THE IMMUNOLOGICAL BASIS OF ACQUIRED CELLULAR RESISTANCE. *J. Exp. Med.* **120**, 105–120 (1964).
21. Liew, F. Y., Li, Y. & Millott, S. Tumor necrosis factor-alpha synergizes with IFN-gamma in mediating killing of Leishmania major through the induction of nitric oxide. *J. Immunol. Baltim. Md 1950* **145**, 4306–4310 (1990).

643 22. Hung, K. *et al.* The Central Role of CD4+ T Cells in the Antitumor Immune Response. *J. Exp.*
644 *Med.* **188**, 2357–2368 (1998).
645 23. Pardoll, D. M. & Topalian, S. L. The role of CD4+ T cell responses in antitumor immunity. *Curr.*
646 *Opin. Immunol.* **10**, 588–594 (1998).
647 24. Borst, J., Ahrends, T., Bąbała, N., Melief, C. J. M. & Kastenmüller, W. CD4+ T cell help in
648 cancer immunology and immunotherapy. *Nat. Rev. Immunol.* **18**, 635–647 (2018).
649 25. Bauer, C. A. *et al.* Dynamic Treg interactions with intratumoral APCs promote local CTL
650 dysfunction. *J. Clin. Invest.* **124**, 2425–2440 (2014).
651 26. Mumberg, D. *et al.* CD4⁺ T cells eliminate MHC class II-negative cancer cells in vivo by
652 indirect effects of IFN-γ. *Proc Natl Acad Sci USA* **96**, 8633–8638 (1999).
653 27. Qin, Z. & Blankenstein, T. CD4⁺ T Cell–Mediated Tumor Rejection Involves Inhibition of
654 Angiogenesis that Is Dependent on IFNγ Receptor Expression by Nonhematopoietic Cells.
655 *Immunity* **12**, 677–686 (2000).
656 28. Corthay, A. *et al.* Primary antitumor immune response mediated by CD4+ T cells. *Immunity*
657 **22**, 371–383 (2005).
658 29. Perez-Diez, A. *et al.* CD4 cells can be more efficient at tumor rejection than CD8 cells. *Blood*
659 **109**, 9 (2007).
660 30. Quezada, S. A. *et al.* Tumor-reactive CD4+ T cells develop cytotoxic activity and eradicate
661 large established melanoma after transfer into lymphopenic hosts. *J. Exp. Med.* **207**, 637–650
662 (2010).
663 31. LaCasse, C. J. *et al.* Th-1 Lymphocytes Induce Dendritic Cell Tumor Killing Activity by an IFN-
664 γ–Dependent Mechanism. *J. Immunol.* **187**, 6310–6317 (2011).
665 32. Braumüller, H. *et al.* T-helper-1-cell cytokines drive cancer into senescence. *Nature* **494**, 361–
666 365 (2013).
667 33. Landsberg, J. *et al.* Melanomas resist T-cell therapy through inflammation-induced reversible
668 dedifferentiation. *Nature* **490**, 412–416 (2012).
669 34. Overwijk, W. W. *et al.* Tumor Regression and Autoimmunity after Reversal of a Functionally
670 Tolerant State of Self-reactive CD8+ T Cells. *J. Exp. Med.* **198**, 569–580 (2003).
671 35. Muranski, P. *et al.* Tumor-specific Th17-polarized cells eradicate large established melanoma.
672 *Blood* **112**, 362–373 (2008).
673 36. Kohlmeyer, J. *et al.* Complete Regression of Advanced Primary and Metastatic Mouse
674 Melanomas following Combination Chemoimmunotherapy. *Cancer Res.* **69**, 6265–6274 (2009).
675 37. Foulds, K. E. *et al.* Cutting edge: CD4 and CD8 T cells are intrinsically different in their
676 proliferative responses. *J. Immunol. Baltim. Md 1950* **168**, 1528–1532 (2002).
677 38. Mengoni, M., Braun, A. D., Gaffal, E. & Tüting, T. The aryl hydrocarbon receptor promotes
678 inflammation-induced dedifferentiation and systemic metastatic spread of melanoma cells. *Int. J.*
679 *Cancer* **147**, 2902–2913 (2020).
680 39. Ferris, S. T. *et al.* cDC1 prime and are licensed by CD4+ T cells to induce anti-tumour
681 immunity. *Nature* **584**, 624–629 (2020).
682 40. Cabeza-Cabrerizo, M., Cardoso, A., Minutti, C. M., Pereira da Costa, M. & Reis e Sousa, C.
683 Dendritic Cells Revisited. *Annu. Rev. Immunol.* **39**, 131–166 (2021).
684 41. Lindquist, R. L. *et al.* Visualizing dendritic cell networks in vivo. *Nat. Immunol.* **5**, 1243–1250
685 (2004).
686 42. Fauskanger, M., Haabeth, O. A. W., Skjeldal, F. M., Bogen, B. & Tveita, A. A. Tumor Killing by
687 CD4+ T Cells Is Mediated via Induction of Inducible Nitric Oxide Synthase-Dependent Macrophage
688 Cytotoxicity. *Front. Immunol.* **9**, 1684 (2018).
689 43. Karki, R. *et al.* Synergism of TNF-α and IFN-γ Triggers Inflammatory Cell Death, Tissue
690 Damage, and Mortality in SARS-CoV-2 Infection and Cytokine Shock Syndromes. *Cell* **184**, 149-
691 168.e17 (2021).
692 44. McGranahan, N. *et al.* Allele-Specific HLA Loss and Immune Escape in Lung Cancer
693 Evolution. *Cell* **171**, 1259-1271.e11 (2017).
694 45. Haabeth, O. A. W. *et al.* CD4 ⁺ T-cell–Mediated Rejection of MHC Class II–Positive Tumor
695 Cells Is Dependent on Antigen Secretion and Indirect Presentation on Host APCs. *Cancer Res.* **78**,
696 4573–4585 (2018).

46. Müller, A. J. *et al.* CD4+ T cells rely on a cytokine gradient to control intracellular pathogens beyond sites of antigen presentation. *Immunity* **37**, 147–157 (2012).
47. Olekhnovitch, R., Ryffel, B., Müller, A. J. & Bousso, P. Collective nitric oxide production provides tissue-wide immunity during Leishmania infection. *J. Clin. Invest.* **124**, 1711–1722 (2014).
48. Badrinath, S. *et al.* A vaccine targeting resistant tumours by dual T cell plus NK cell attack. *Nature* (2022) doi:10.1038/s41586-022-04772-4.
49. Guilliams, M., Mildner, A. & Yona, S. Developmental and Functional Heterogeneity of Monocytes. *Immunity* **49**, 595–613 (2018).
50. Locati, M., Curtale, G. & Mantovani, A. Diversity, Mechanisms, and Significance of Macrophage Plasticity. *Annu. Rev. Pathol. Mech. Dis.* **15**, 123–147 (2020).
51. Bosteels, C. *et al.* Inflammatory Type 2 cDCs Acquire Features of cDC1s and Macrophages to Orchestrate Immunity to Respiratory Virus Infection. *Immunity* **52**, 1039-1056.e9 (2020).
52. Simpson, D. S. *et al.* Interferon-γ primes macrophages for pathogen ligand-induced killing via a caspase-8 and mitochondrial cell death pathway. *Immunity* **55**, 423-441.e9 (2022).
53. Bald, T. *et al.* Ultraviolet-radiation-induced inflammation promotes angiotropism and metastasis in melanoma. *Nature* **507**, 109–113 (2014).
54. Schmid-Burgk, J. L. *et al.* OutKnocker: a web tool for rapid and simple genotyping of designer nuclease edited cell lines. *Genome Res.* **24**, 1719–1723 (2014).
55. Bernstein, N. J. *et al.* Solo: Doublet Identification in Single-Cell RNA-Seq via Semi-Supervised Deep Learning. *Cell Syst.* **11**, 95-101.e5 (2020).
56. Lun, A. T. L., McCarthy, D. J. & Marioni, J. C. A step-by-step workflow for low-level analysis of single-cell RNA-seq data with Bioconductor. *F1000Research* **5**, 2122 (2016).
57. Wolf, F. A., Angerer, P. & Theis, F. J. SCANPY: large-scale single-cell gene expression data analysis. *Genome Biol.* **19**, 15 (2018).
58. Aran, D. *et al.* Reference-based analysis of lung single-cell sequencing reveals a transitional profibrotic macrophage. *Nat. Immunol.* **20**, 163–172 (2019).
59. Bergen, V., Lange, M., Peidli, S., Wolf, F. A. & Theis, F. J. Generalizing RNA velocity to transient cell states through dynamical modeling. *Nat. Biotechnol.* **38**, 1408–1414 (2020).

Acknowledgements

We would like to thank the following individuals for their support:

S. Bonifatius, J. Herz, J. Leipold, A. Ziems, K. Beinhoff , R. Hartig, J. Dudeck for managing the mouse colony, performing tumour analyses, and assisting for intravital microscopy and cell sorting.

T.T. was supported by funding from the German Research Foundation (DFG Projects SFB854-P27 and SFB704-P22) and the German Cancer Aid (Deutsche Krebshilfe Nr. 70112525). A.J.M. was supported by funding from the European Research Council (ERC) under the European Union's Horizon 2020 research and innovation program (StG ImmProDynamics, grant agreement 714233) and the German Research Foundation DFG (SFB854-Z01, SFB854-B31). A.B. and M.M. were funded by the Else Kröner-Fresenius Forschungskolleg Magdeburg (2017_Kolleg.07; TP3 and TP4).

Author contributions

BK, ACB, NS, SG, KK, SH, YF, TV, AK performed experiments and analysed data. BK, NS, JP, JR generated cell lines. NS, DY, ME generated the adenovirus construct. MM, AB collected clinical data.

AB, RG performed single cell RNA sequencing analyses. BK, ACB, NS, SG, AJM, TT designed experiments. BK, ACB, NS, AB, EG, SK, DM, HK, WK, AJM, TT contributed intellectual input and helped to interpret data. AJM, TT led the research program. BK, ACB, WK, AJM, TT wrote the manuscript.

Kruse et al. Figure 1

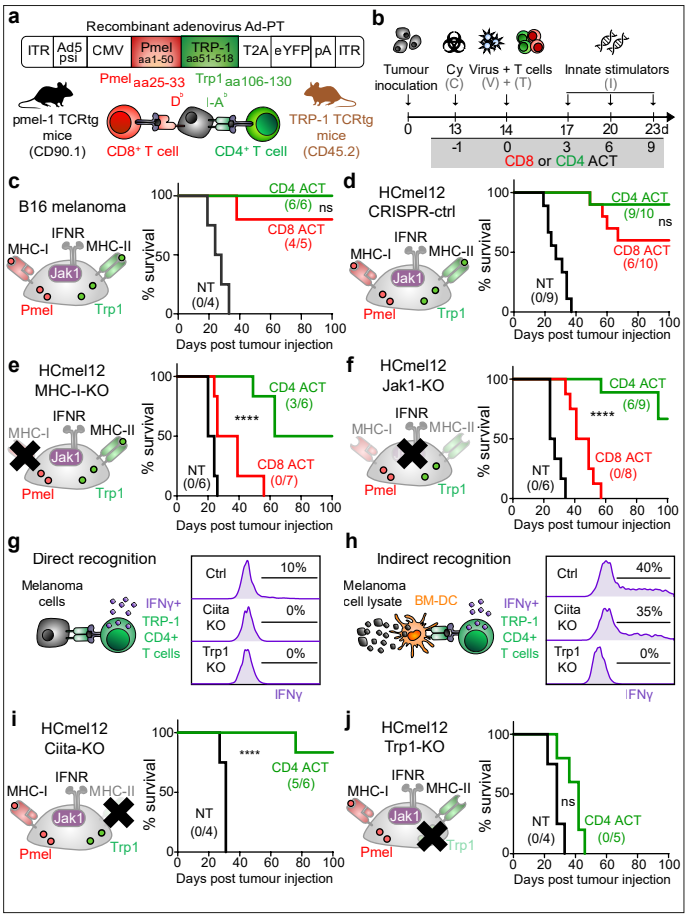

Fig. 1 | CD4+ effector T cells eradicate MHC-deficient and IFN-unresponsive melanomas that resist destruction by CD8+ cytotoxic T cells.

a, Structure of recombinant Ad-PT virus designed to simultaneously stimulate pmel-1 CD8⁺ and TRP-1 CD4⁺ TCRtg T cells. **b**, Experimental protocol for adoptive cell transfer (ACT) therapy of established tumours in mice consisting of cyclophosphamide pre-conditioning (Cy, C) one day before vaccination with Ad-PT (V) and adoptive transfer of TCRtg T cells (T) followed by intra-tumoural injections with polyI:C and CpG (Innate stimuli, I). **c-f, i, j**, Graphical representation of the genetic phenotype of the indicated melanoma cells (left) and Kaplan-Meier survival curves of mice bearing established melanomas and treated as indicated (number of surviving mice in parenthesis). **g**, **h**, Graphical representation of direct (g) and indirect (h) recognition of melanoma cells by CD4+ T cells (left) and representative flow cytometry histograms showing IFNg⁺ TRP-1 CD4+ T cells following stimulation by the indicated melanoma cells (right). Survival was statistically compared using log-rank Mantel-Cox test, ****p<0.0001.

Kruse et al. Figure 2

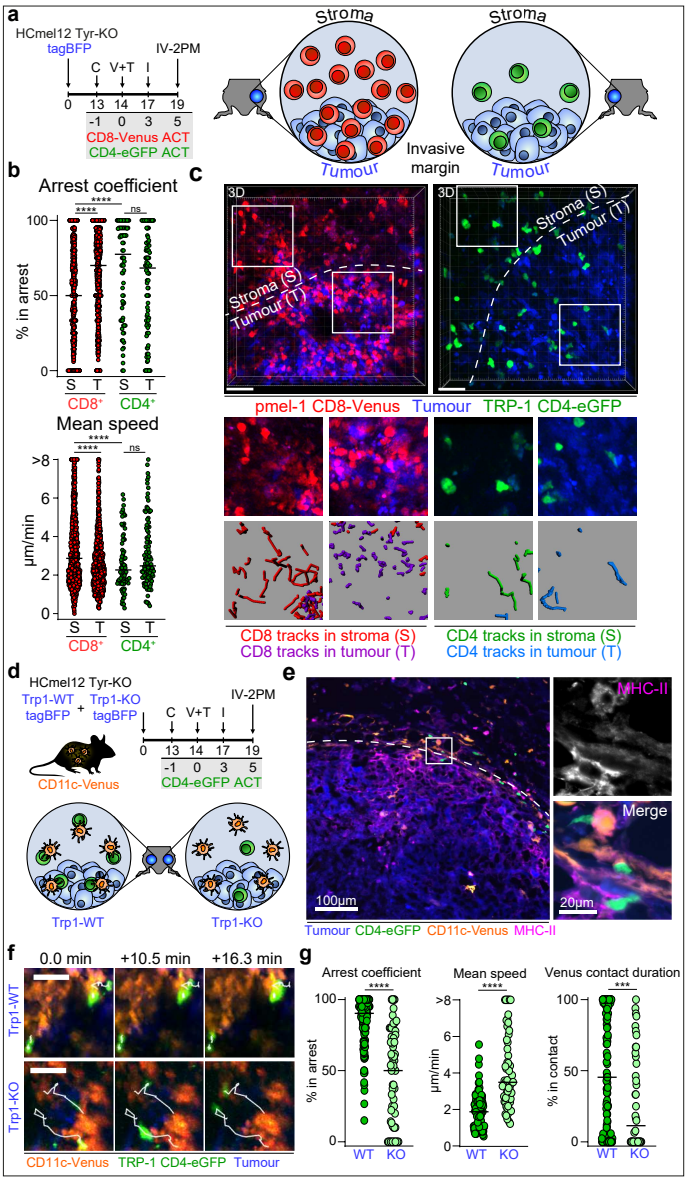

Fig. 2 | CD4+ effector T cells preferentially migrate within the invasive tumour margin where they form antigen-dependent local clusters with MHC-II-expressing CD11c+ immune cells.

a, Experimental protocol for intravital 2-photon microscopy (IV-2PM) of tagBFP-labelled HCmel12 *Tyr*-KO (amelanotic) melanomas treated with pmel-1 CD8-Venus or TRP-1 CD4-eGFP T cells (left) and graphical representation of adoptively transferred T cells at the invasive margin (right). **b**, Arrest coefficient and mean speed of adoptively transferred pmel-1 CD8-Venus (left) and TRP-1 CD4-eGFP T cells (right) in the stromal (S) and tumoural (T) compartment at the invasive margin (the bar indicates the median). **c**, Representative intravital microscopic images (top) and examples for real-time tracking of pmel-1 CD8-Venus (left) and TRP-1 CD4-eGFP T cells (right) at the invasive tumour margin. **d**, Experimental protocol to assess antigen-dependent interactions between TRP-1 CD4-eGFP T cells and CD11c+ immune cells in CD11c-Venus mice bearing *Trp1*-WT and *Trp1*-KO melanomas. **e**, Representative immunofluorescence microscopic image of an MHC-II-stained cryosection from a *Trp1*-WT melanoma. **f**, Representative intravital microscopic images of TRP-1 CD4-eGFP T cells interacting with CD11c-Venus cells in *Trp1*-WT and *Trp1*-KO melanomas. **g**, Arrest coefficient, mean speed, and relative contact duration between TRP-1 CD4-eGFP T cells and CD11c-Venus cells (the bar indicates the median). Data were pooled from at least two biologically independent experiments and groups statistically compared using a two-way ANOVA with Tukey post-hoc ***p<0.001, ****p<0.0001.

Kruse et al. Figure 3

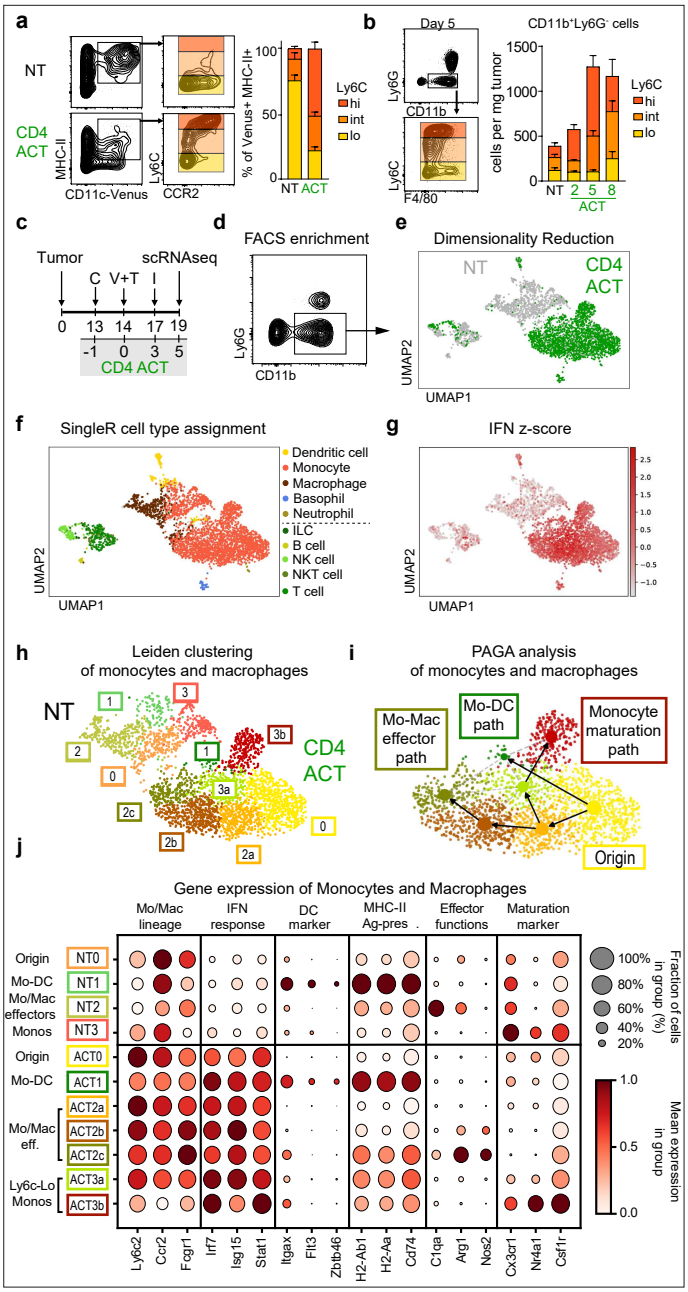

Fig. 3 | CD4+ effector T cells and innate immune stimulation promote the recruitment of inflammatory monocytes into tumour tissues and drive the acquisition of IFN-activated effector phenotypes.

a. Representative flow cytometric contour plots showing the gating strategy to assess the phenotype of CD11c-Venus+ MHC-II+ immune cells isolated from melanomas on day 5 after CD4+ T cell transfer compared to controls (left), distribution of Ly6C expression (right). **b**, Representative flow cytometric contour plots showing the gating strategy to assess the distribution of Ly6C expression on CD11b+LygG- cells (left) and the quantification (right) in melanomas 2, 5, and 8 days after CD4+ T cell transfer compared to non-treated (NT). **c**, Experimental protocol for a scRNAseq analysis. **d**, Representative flow cytometric contour plot showing enrichment of CD11b$^+$ Ly6G$^-$ cells from single cell suspensions of CD45+ tumour-infiltrating immune cells. **e**, Visualisation and dimensionality reduction of scRNAseq data using uniform manifold approximation and projection (UMAP) comparing samples from CD4 ACT-treated and non-treated (NT) mice. **f-h**, Corresponding UMAP plots showing automatically assigned cell types using SingleR (f), the expression of an IFN-induced gene set as IFN z-score (g) and graph-based clustering using the Leiden algorithm (h). **i**, Pseudotime inference using scVelo and graph abstraction using PAGA for monocytes of CD4-ACT-treated melanomas. **j**, Bubble plot showing expression levels of selected signature genes for the individual Leiden clusters arranged according to the developmental trajectories. Dot size indicates fraction of expressing cells, colours are based on normalised expression levels.

Kruse et al. Figure 4

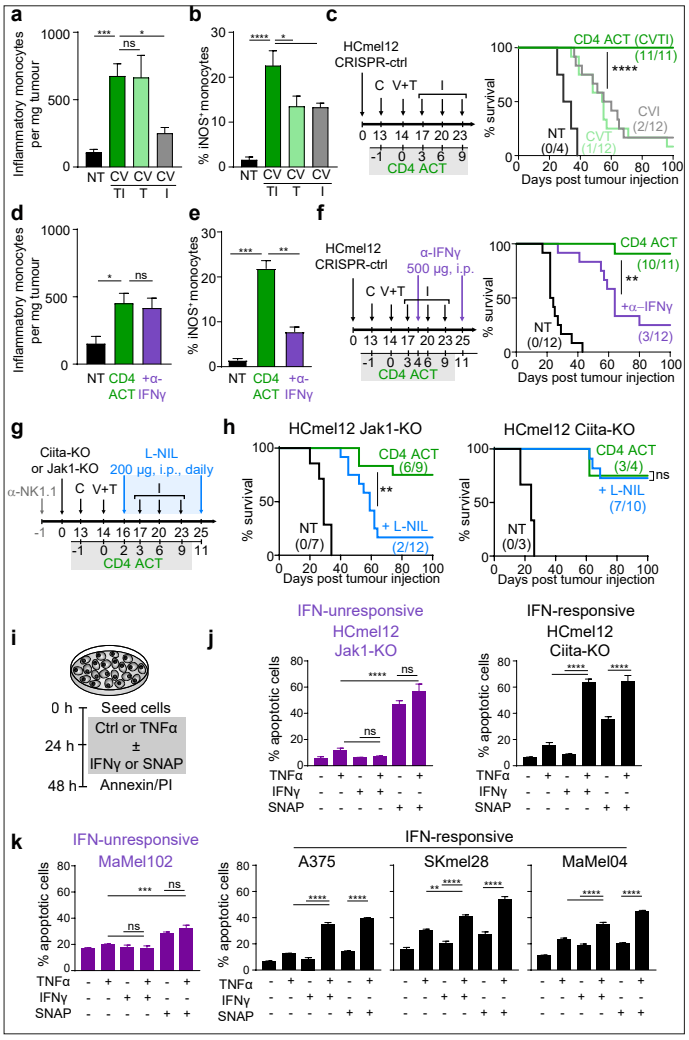

Fig. 4 | CD4+ effector T cells and innate immune stimulation synergistically activate tumouricidal monocytes and orchestrate indirect inflammatory killing of MHC-deficient and IFN-unresponsive tumours.

a, **d**, Quantification of tumour-infiltrating inflammatory monocytes in established HCmel12 CRISPR-ctrl melanomas treated as indicated (± SEM, n=11-12). **b**, **e**, Corresponding quantification of iNOS-expressing monocytes (± SEM). **c**, **f-h**, Experimental treatment protocols (left) and Kaplan-Meier survival curves of mice bearing established melanomas and treated as indicated (number of surviving mice in parenthesis). **i**, Experimental protocol to assess the ability of the inflammatory mediators TNFα, IFNγ and the nitric oxide donor SNAP to induce melanoma cell apoptosis. **j**, **k**, Quantification of apoptotic melanoma cells treated as indicated (± SEM). Data were pooled from at least two biologically independent experiments. Survival was statistically compared using log-rank Mantel-Cox test. Means between groups were statistically compared using a one-way ANOVA with Tukey post-hoc, *p<0.05, **p<0.01, ***p<0.001, ****p<0.0001.

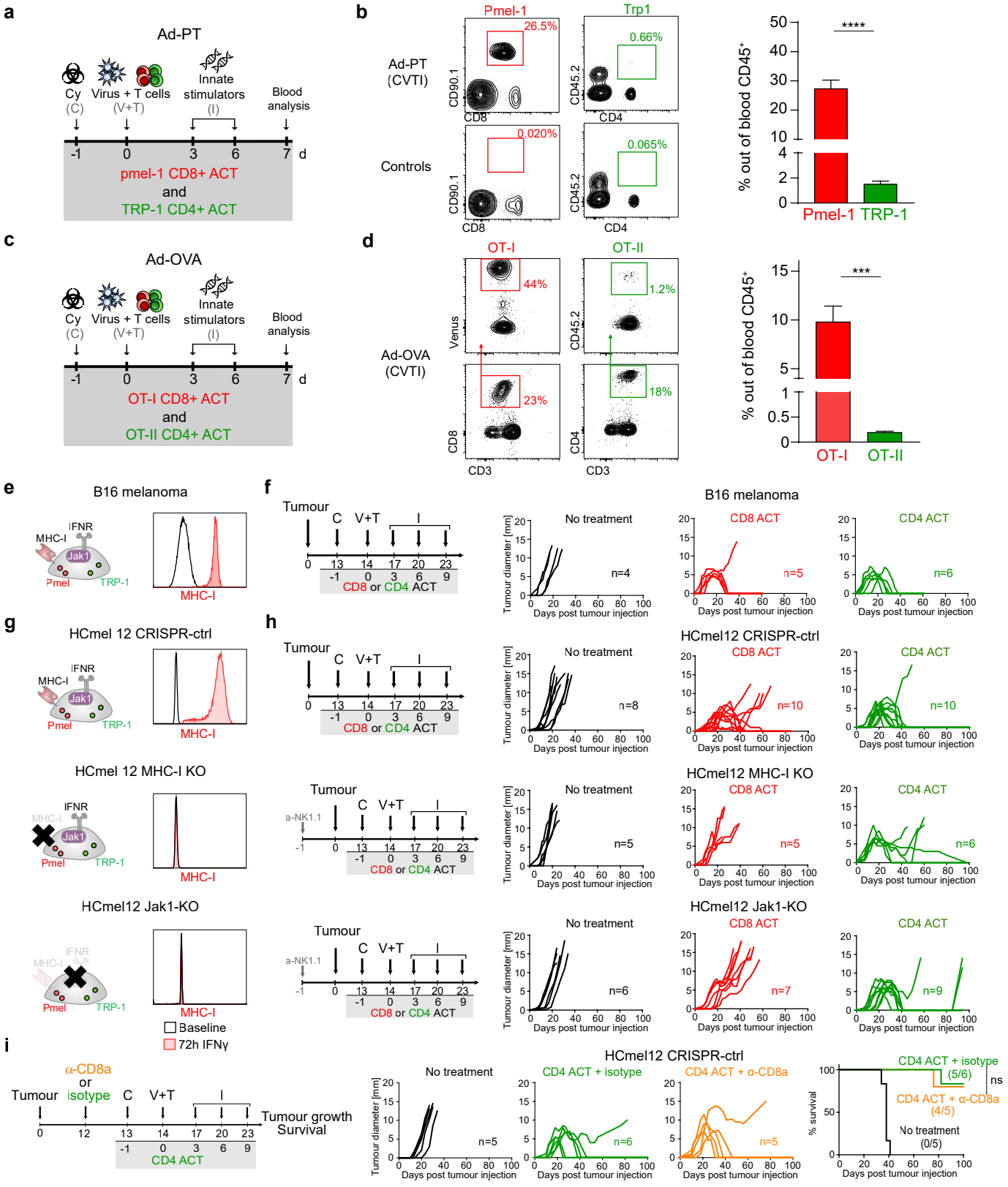

Extended Data Fig. 1 | CD4+ T cells eradicate MHC-I-deficient and IFN-unresponsive that resist destruction by cytotoxic CD8+ T cells in the same experimental adoptive T cell transfer setting.

Extended Data Fig. 1 | CD4+ T cells eradicate MHC-I-deficient and IFN-unresponsive that resist destruction by cytotoxic CD8+ T cells in the same experimental adoptive T cell transfer setting.

a, **c**, Experimental protocol to assess the expansion of adoptively transferred pmel-1 CD8+ and TRP-1 CD4+ TCRtg T cells (a) or ovalbumin-specific OT-I CD8+ and OT-II CD4+ TCRtg T cells (c) in peripheral blood 7 days after ACT. **b**, **d**, Representative flow cytometric dot plots identifying expanded T cells in blood (left) and cumulative results ± SEM (right) from mice treated as indicated. **e**, **g**, Graphical representation of the genetic phenotype of the indicated melanoma cells (left) and representative flow cytometric histograms for MHC-I expression in the presence or absence of IFNg. **f**, **h**, Experimental treatment protocol (left) and individual tumour growth curves of mice bearing established melanomas and treated as indicated. **i**, Experimental treatment protocol (left), individual tumour growth curves of mice bearing HCmel12 CRISPR-Ctrl melanomas treated as indicated (middle) and Kaplan-Meier survival graph (right, number of surviving mice in parenthesis). Data shown is from a single representative experiment and has been repeated independently at least twice. Means in (b) and (d) were statistically compared using a paired student's t test. Survival was statistically compared using log-rank Mantel-Cox test. ***p<0.001, ****p<0.0001.

Kruse et al. Extended Data Fig. 2

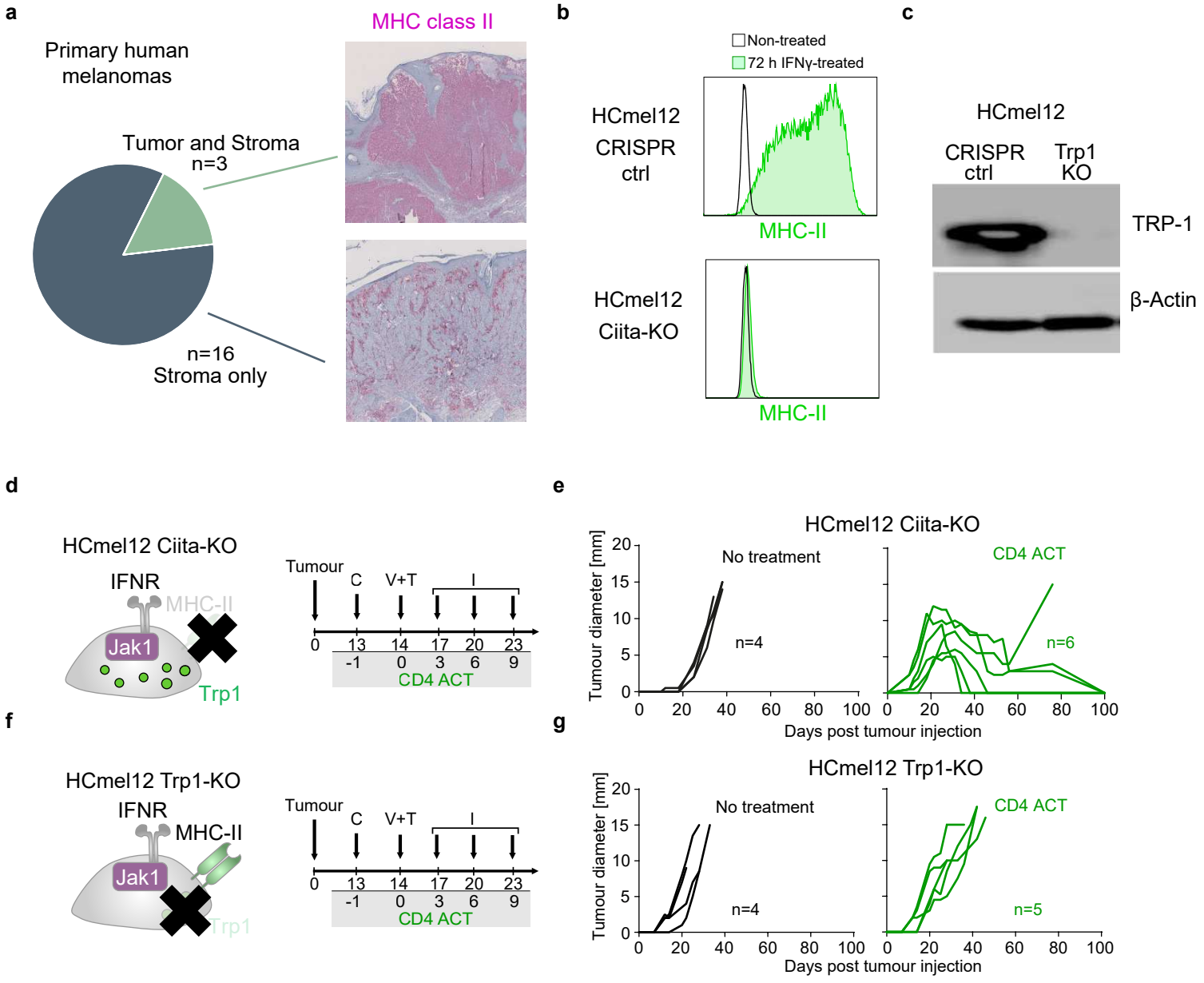

Extended Data Fig. 2 | CD4+ effector T cells eradicate established MHC class II-deficient HCmel12 melanomas through indirect antigen-specific activation in the tumour microenvironment.

a, Summary of primary human melanoma specimens immunohistochemically stained for MHC-II (left) and representative images (right). **b**, Representative flow cytometric histograms for MHC-II expression on indicated melanoma cells in the presence or absence of IFNγ. **c**, Western blot analysis for TRP-1 expression for the indicated melanoma cells. **d**, **f**, Graphical representation of the genetic phenotype of the indicated melanoma cells (left) and experimental treatment protocols (right). **e**, **g**, Individual tumour growth curves of representative groups of mice bearing established melanomas and treated as indicated.

Kruse et al. Extended Data Fig. 3

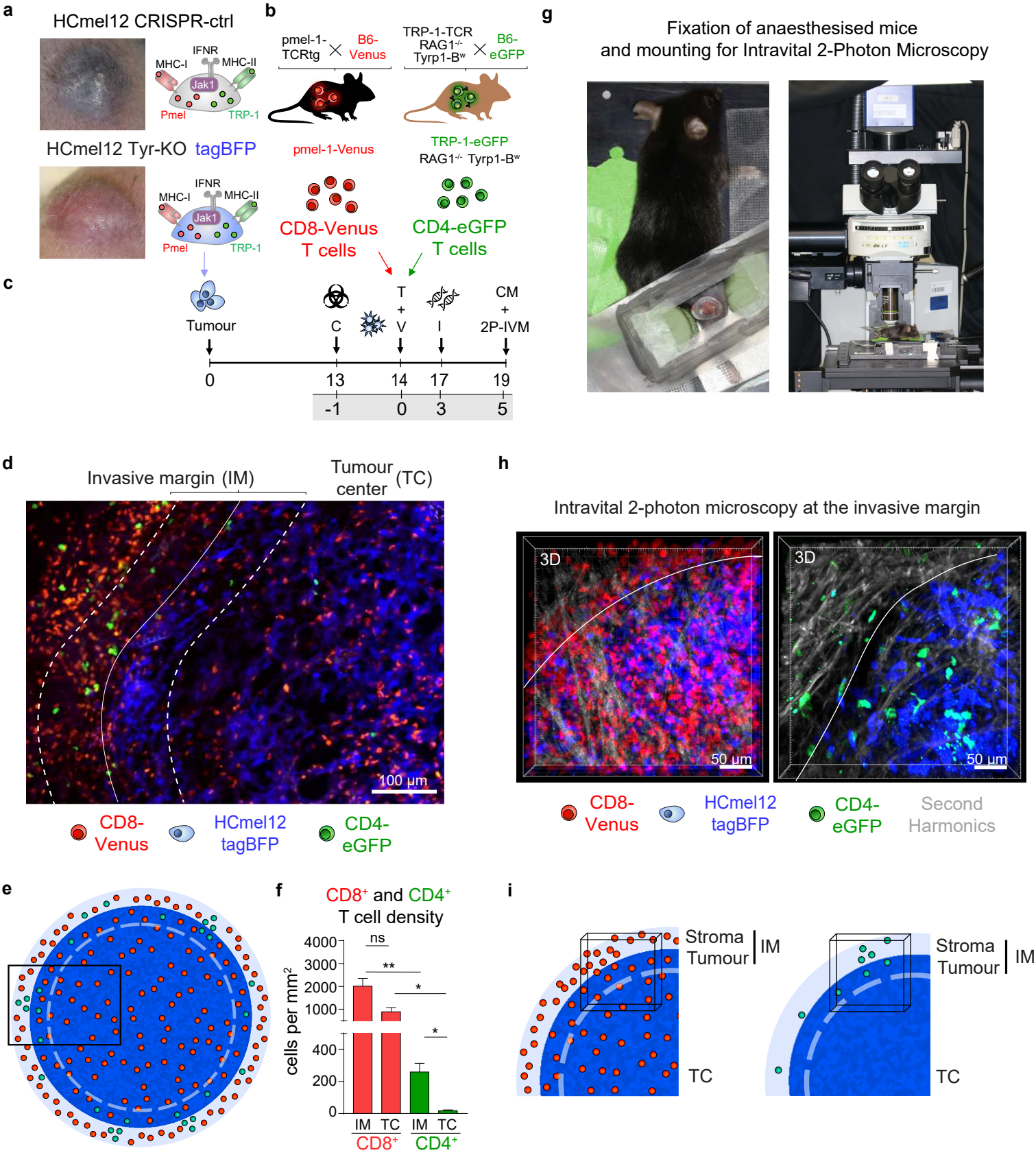

Extended Data Fig. 3 | CD4+ effector T cells show a different spatial distribution and migratory behaviour in tumour tissues when compared to CD8+ effector T cells..

Extended Data Fig. 3 | CD4+ effector T cells show a different spatial distribution and migratory behaviour in tumour tissues when compared to CD8+ effector T cells.

a, Photographic images of established tumours (left) and graphical representations (right) of the genetic phenotype of the indicated melanomas (bottom). **b**, Breeding scheme to generate pmel-1 Venus and TRP-1 eGFP TCRtg mice. **c**, Experimental protocol for immunofluorescence and intravital 2-photon microscopy (IV-2PM) of tagBFP-labelled HCmel12 *Tyr*-KO melanomas treated with pmel-1 CD8-Venus or TRP-1 CD4-eGFP T cells. **d**, Representative fluorescence microscopic image of pmel-1 CD8-Venus T cells and TRP-1 CD4-eGFP T cells in tagBFP-labelled HCmel12 *Tyr*-KO melanomas. **e**, Diagrammatic representation of the T cell distribution in a whole tumour cryosection. **f**, Corresponding quantification of pmel-1 CD8-Venus and TRP-1 CD4-eGFP T cell density at the invasive margin (IM) and in the tumour centre (TC) of a tagBFP-labelled HCmel12 *Tyr*-KO melanoma (± SEM). **g**, Photographic images of the experimental setup for intravital 2-photon microscopy. **h**, Representative intravital microscopic images for pmel-1 CD8-Venus (left) and TRP-1 CD4-eGFP T cells (right) at the invasive tumour margin. Data in (f) were pooled from two biologically independent experiments. Means between groups were statistically compared using a one-way ANOVA with Tukey post-hoc, *$p<0.05$, **$p<0.01$.

Kruse et al. Extended Data Fig. 4

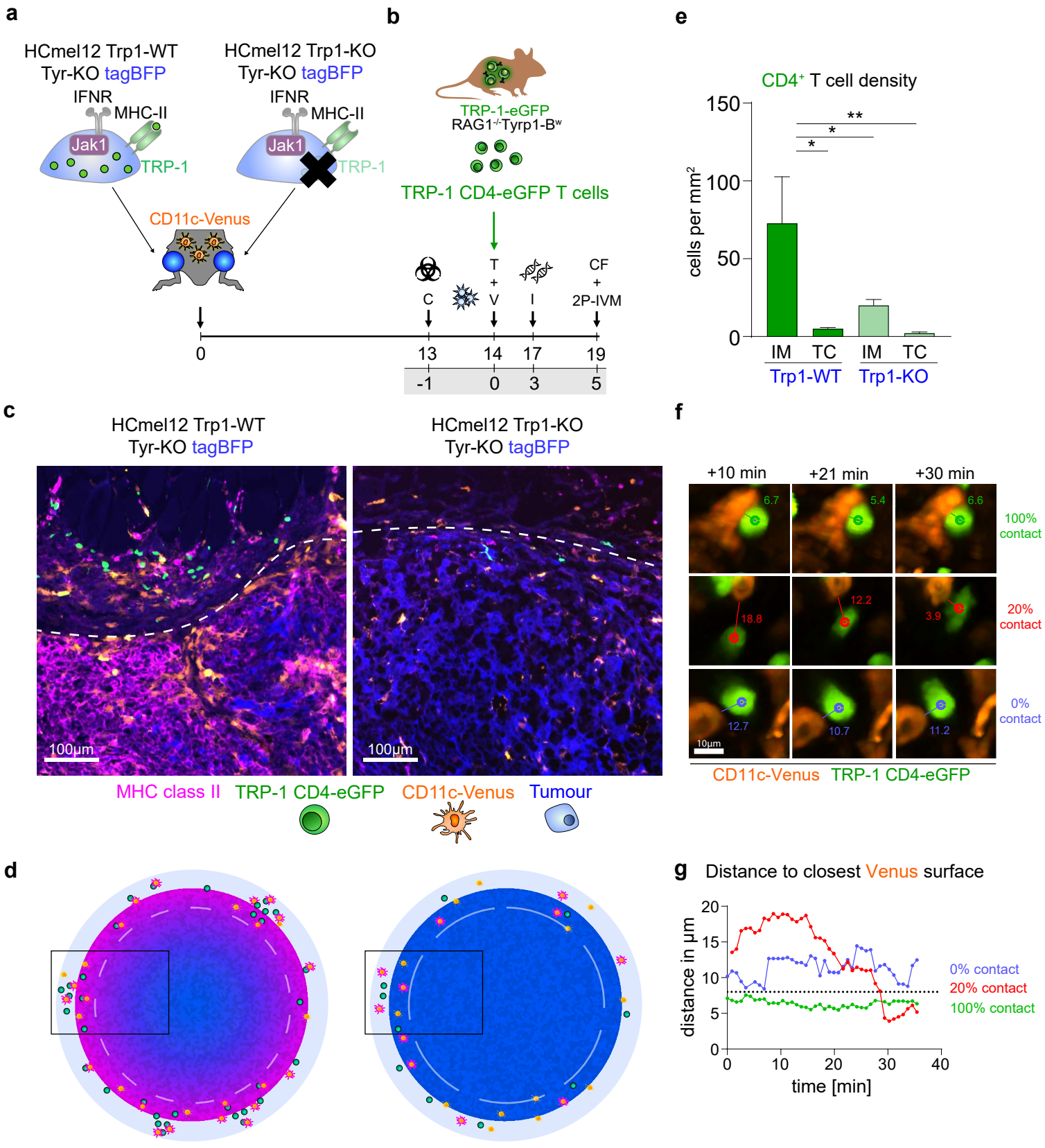

Extended Data Fig.4 | CD4+ effector T cells interact with MHC II-expressing CD11c+ immune cells in local clusters at the invasive tumour margin.

Extended Data Fig. 4 | CD4+ effector T cells interact with MHC-II-expressing CD11c+ immune cells in local clusters at the invasive tumour margin.

a, **b**, Graphical representation (upper left) of the genetic phenotype of the indicated melanomas and experimental protocol to study antigen-specific interactions between TRP-1 CD4-eGFP T cells and CD11c+ cells in CD11c-Venus mice. **c**, Representative immunofluorescence microscopic images of MHC-II-stained cryosections from a *Trp1*-WT (left) and a *Trp1*-KO melanoma (right). **d**, Diagrammatic representation of MHC-II expression (magenta) and interactions between TRP-1 CD4-eGFP T cells and CD11c-Venus antigen-presenting cells in corresponding whole tumour cryosections. **e**, Corresponding quantification of TRP-1 CD4-eGFP T cell density at the invasive margin (IM) and in the tumour centre (TC) of in *Trp1*-WT and *Trp1*-KO melanomas. **f**, Representative intravital microscopic images to measure the distance between TRP-1 CD4-eGFP T cells and CD11c-Venus cells. **g**, Corresponding contact duration over time. Data in (e) were pooled from two biologically independent experiments. Means between groups were statistically compared using a one-way ANOVA with Tukey post-hoc, *p<0.05, **p<0.01.

Kruse et al. Extended Data Fig. 5

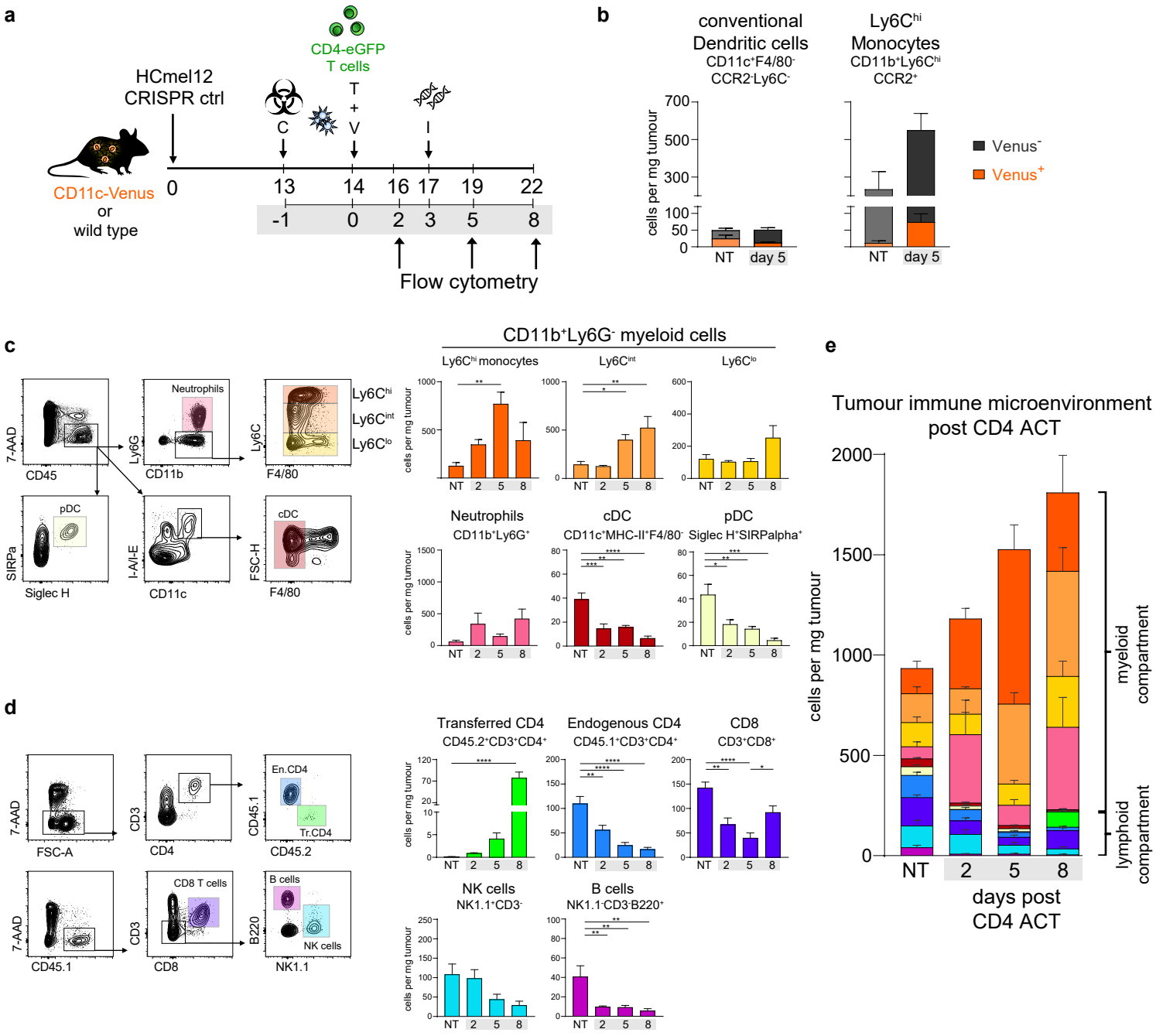

Extended Data Fig. 5 | Flow cytometric profiling of the tumour immune microenvironment reveals a rapid recruitment of inflammatory monocytes in CD4 ACT-treated mice.

a, Experimental protocol to characterise tumour-infiltrating immune cells in non-treated and CD4 ACT-treated HCmel12 CRISPR-ctrl melanomas over time. **b**, Quantification of dendritic cells and inflammatory monocytes in melanomas of CD11c-Venus mice following CD4 ACT therapy compared to controls. **c**, **d**, Representative flow cytometric contour plots showing the gating strategy to comprehensively quantify tumour-infiltrating myeloid (c) and lymphoid (d) immune cell subsets (left) and cumulative results (right) for the indicated cell types over time (± SEM). **e**, Compilation of all tumour-infiltrating immune cell subsets. Data were pooled from at least two biologically independent experiments. Means between groups were compared statistically using a one-way ANOVA with Tukey post-hoc, *p<0.05, **p<0.01, ***p<0.001, ****p<0.0001.

Kruse et al. Extended Data Fig. 6

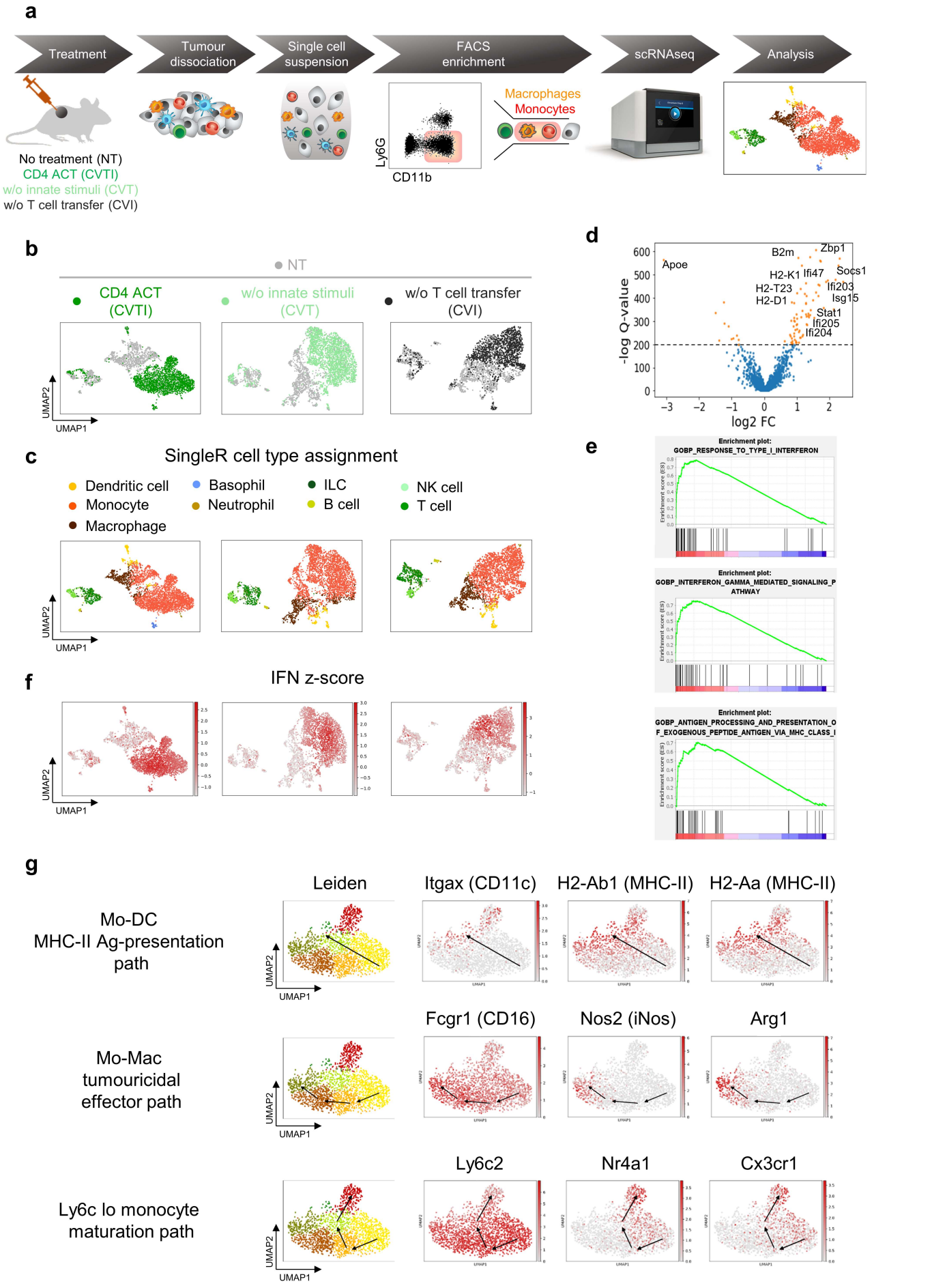

Extended Data Fig. 6 | Single cell RNAseq analyses demonstrate that tumour-infiltrating inflammatory monocytes acquire IFN-activated effector phenotypes upon therapy.

a, Schematics of the workflow for single cell RNA sequencing of intratumoural CD11b+Ly6G- immune cells. **b,** Visualisation and dimensionality reduction of scRNAseq data using uniform manifold approximation and projection (UMAP) comparing samples from the indicated treatment groups individually with non-treated (NT) mice. **c,** Corresponding UMAP plots showing automatically assigned cell types using SingleR. **d,** Volcano plot showing differentially expressed genes comparing samples from CD4 ACT-treated and non-treated (NT) mice. Genes with –log Q-values > 200 are shown in orange. **e,** Enrichment plots from a gene set enrichment analysis of the differentially expressed genes shown in (**d**). Gene ontology pathway sets were considered in the analysis. **f,** UMAP plots showing the expression of an IFN-induced gene set as IFN z-score for the indicated treatment groups. **g,** UMAP plots showing differentiation pathways of monocytes recruited into CD4-ACT-treated melanomas identified by pseudotime inference and graph abstraction (left) and corresponding expression of the indicated characteristic marker genes (right).

Kruse et al. Extended Data Fig. 7

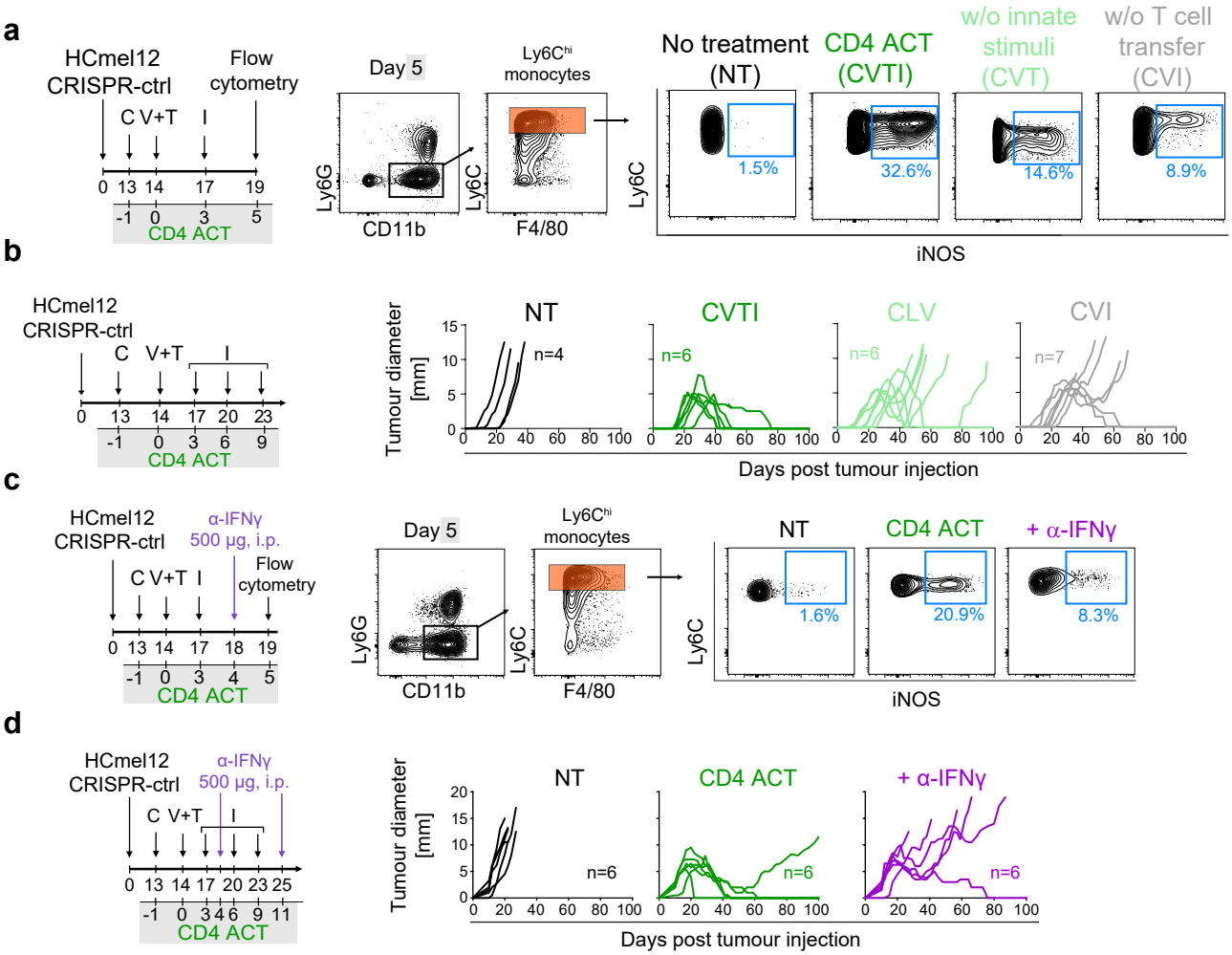

Extended Data Fig. 7 | CD4+ T cells and innate immune stimulation synergistically activate tumouricidal monocytes and drive IFNγ-dependent eradication of established melanomas.

a, **c**, Experimental protocol to analyse tumour-infiltrating immune cells (left), gating strategy to identify inflammatory monocytes (middle) and representative flow cytometric contour plots for iNOS expression (right). **b**, **d**, Experimental treatment protocols (left) and individual growth curves of representative groups of mice bearing established melanomas and treated as indicated.

Kruse et al. Extended Data Fig. 8

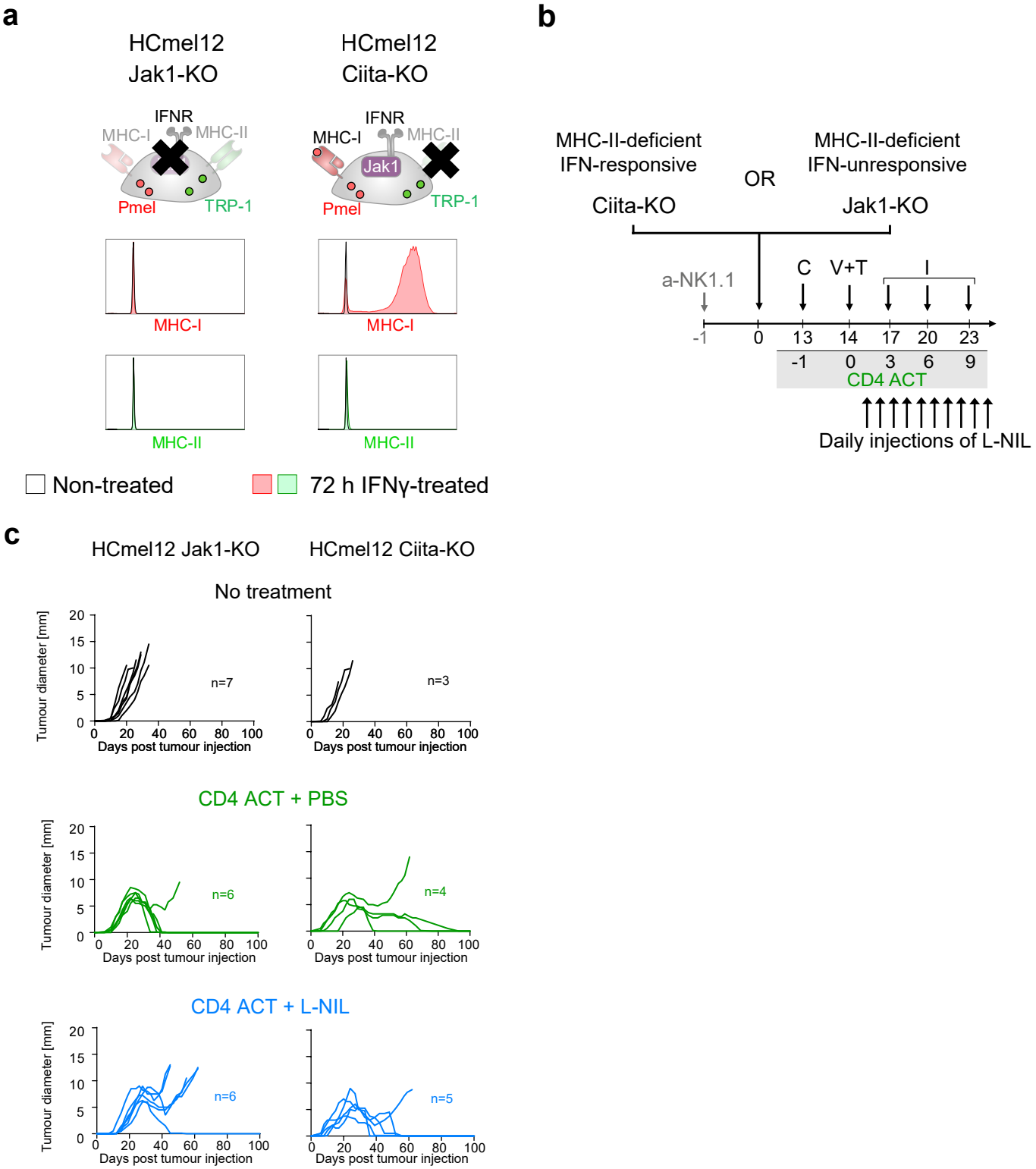

Extended Data Fig. 8 | IFNγ-induced nitric oxide production by myeloid cells is essential for indirect recognition and destruction of established IFN-unresponsive and MHC-deficient melanomas by CD4+ T effector cells.

a, Graphical representation of the genetic phenotype of the indicated melanoma cells (top) and representative flow cytometric histograms for MHC-I and MHC-II expression in the presence or absence of IFNγ (bottom). **b**, Experimental treatment protocol. **c**, Individual tumour growth curves of representative groups of mice bearing established melanomas and treated as indicated (L-NIL ~ iNOS inhibitor).

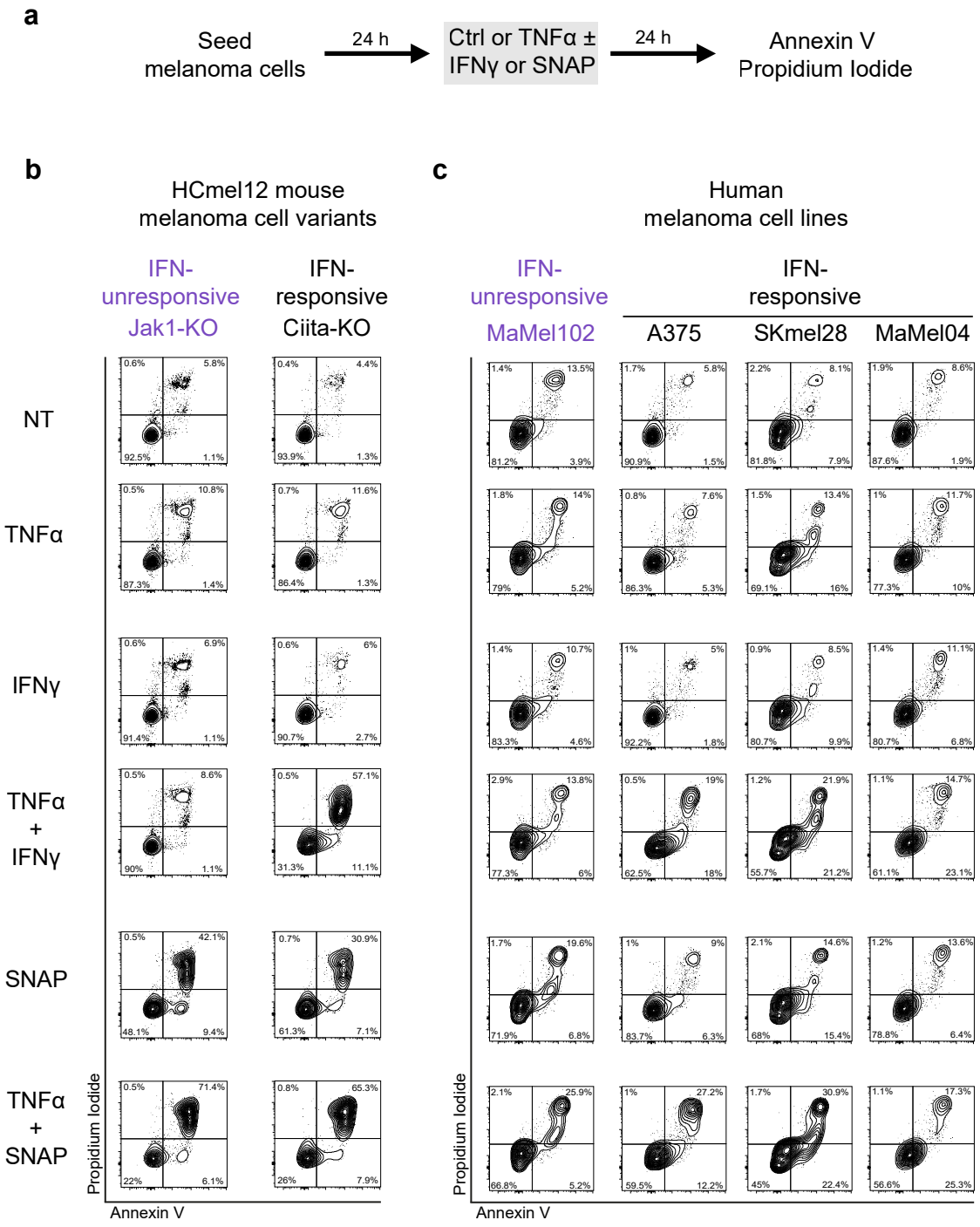

Extended Data Fig. 9 | Nitric oxide induces apoptotic cell death of IFN-unresponsive melanoma cells and complements the ability of IFNγ to sensitise IFN-responsive melanoma cells for TNFα-induced apoptotic cell death.

a, Experimental protocol to assess the ability of the inflammatory mediators TNFα, IFNγ and the nitric oxide donor SNAP to induce melanoma cell apoptosis. **b, c**, Representative flow cytometric contour plots for apoptosis detection of mouse and human melanomas treated as indicated.

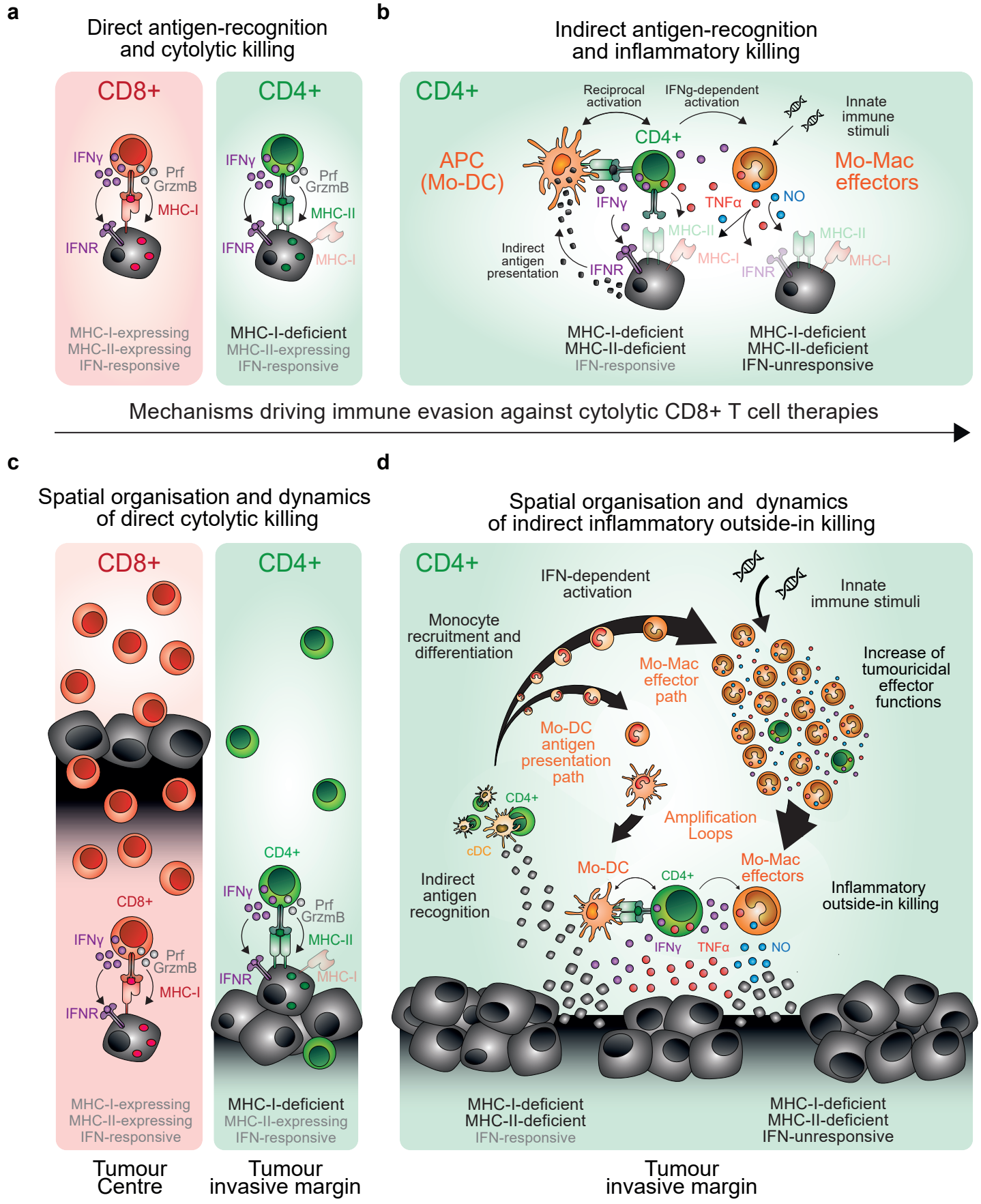

Extended Data Fig. 10 | Spatial organisation and dynamics of T cell effector functions in tumour tissues.

Extended Data Fig. 10 | Spatial organisation and dynamics of T cell effector functions in tumour tissues.

a, Graphical representation of direct antigen recognition and cytolytic killing. CD8+ and CD4+ effector T cells can recognise their antigens as peptide epitopes presented by MHC-molecules on tumour cell surfaces and initiate direct killing through the release of cytolytic granules. **b**, Graphical representation of indirect antigen recognition and inflammatory killing. CD4+ effector T cells also efficiently recognise tumour antigen on the surface of antigen-presenting cells (APC) including monocyte-derived dendritic cells (Mo-DC) and engage tumouricidal effector cells of the monocyte-macrophage lineage (Mo-Mac effectors) to initiate indirect killing through the release of pro-apoptotic inflammatory mediators. **c**, Spatial organisation and dynamics of direct cytolytic killing. CD8+ effector T cells briskly infiltrate tumour tissues where they directly interact with tumour cells (left), while CD4+ effector T cells directly interact with tumour cells mainly near the invasive margin (right). **d,** Spatial organisation and dynamics of inflammatory killing. CD4+ effector T cells cluster locally at the tumour invasive margin, where they indirectly recognise tumour antigen phagocytosed, processed and presented by dendritic cells. Activated CD4+ T cells secrete IFNγ leading to the recruitment and activation of monocytes into the tumour tissue. IFN-activated monocytes phenotypically develop along differentiations path towards antigen-presenting monocyte-derived dendritic cells (Mo-DCs) and tumouricidal monocyte-macrophage effector cells (Mo-Mac effectors). Mo-DCs additionally activate CD4+ T cells and amplify monocyte recruitment, activation and differentiation. Innate immune stimulation increases the tumouricidal functions of Mo-Mac effectors. CD4+ T cell-derived IFNγ and Mo-Mac effector-derived nitric oxide (NO) independently promote TNFα-induced apoptotic tumour cell death. This mechanism of indirect inflammatory outside-in killing eradicates IFN-responsive as well as IFN-unresponsive, MHC-deficient tumours that evade direct cytolytic killing.

Video 1 – Pmel-1 CD8+ T cells arrest in proximity to HCmel12 tumour cells

WT mice were inoculated i.c. with HCmel12 Tyr-KO tagBFP+ cells and treated with Venus+ pmel-1 CD8+ T cell ACT after tumours reached a mean diameter of 3 mm. Imaging was performed five days after ACT.

Video 2 – TRP-1 CD4+ T cells arrest in both the tumour and the stroma

WT mice were inoculated i.c. with HCmel12 Tyr-KO tagBFP+ cells and treated with eGFP+ TRP-1 CD4+ T cell ACT after tumours reached a mean diameter of 3 mm. Imaging was performed five days after ACT.

Video 3 – TRP-1 CD4+ T cells arrest in contact to CD11c+ cells at the invasive tumour margin

CD11c-Venus mice were inoculated i.c. with HCmel12 *Tyr*-KO tagBFP+ (*Trp1* WT) and HCmel12 *Tyr*-KO *Trp1*-KO (Trp1 KO) tumours on contralateral hindlegs and treated with eGFP+ TRP-1 CD4+ T cell ACT after tumours reached a mean diameter of 3 mm. Imaging was performed five days after ACT.

Supplementary Files

This is a list of supplementary files associated with this preprint. Click to download.

- KruseetalSupplVideo2CD4Tcells.mov
- KruseetalSupplVideo1CD8Tcells.mov
- KruseetalSupplVideo3CD11cCD4.mov